Pharmacological inhibition of MCL-1 disrupts mitochondrial cristae and depletes the human neural progenitor cell pool

Marina R. Hanna[1], Madison Yarbrough[2], Melanie Gil[1], James Costanzo[2], and Vivian Gama[1,2,3]

[1]Vanderbilt University, Vanderbilt Brain Institute, Nashville, TN
[2]Vanderbilt University, Cell and Developmental Biology, Nashville, TN.
[3]Vanderbilt University, Vanderbilt Center for Stem Cell Biology, Nashville, TN

[5]Corresponding author

Correspondence should be addressed to:

Vivian Gama
465 21st Avenue South
Vanderbilt University
Nashville, TN 37240-7935
vivian.gama@vanderbilt.edu

Keywords: neural stem cells, MCL-1, mitochondria, cristae, MICOS, OPA1, intermediate progenitors

Abstract

Myeloid Cell Leukemia-1 (MCL-1) is canonically an anti-apoptotic protein that is crucial for early neurodevelopment. Loss of MCL-1 results in embryonic-lethal neurodevelopmental defects that cannot be rescued by other anti-apoptotic proteins of the B-cell lymphoma 2 (BCL-2) family. Here, we pharmacologically inhibit MCL-1 in human neural stem cells and find non-apoptotic roles for MCL-1 in sustaining mitochondrial cristae integrity, fatty acid oxidation, and neural progenitor identity. MCL-1 inhibition disrupts mitochondrial ultrastructure, leading to swollen mitochondria with disorganized cristae and destabilization of the OPA1-MICOS machinery that maintains inner membrane architecture. These structural defects are accompanied by impaired lipid droplet accumulation and altered expression of β-oxidation enzymes, revealing a tight link between cristae architecture and metabolic competence. Functionally, in the absence of caspase-mediated cell death, MCL-1 inhibition selectively depletes intermediate progenitor cells without affecting proliferation, indicating a direct role in lineage progression. Together, our findings identify MCL-1 as a modulator of cristae organization, linking lipid metabolism to neural progenitor fate. This work establishes mitochondrial inner membrane architecture as an instructive determinant of human neurogenesis and highlights the non-canonical MCL-1 functions as critical regulators of human brain development.

Introduction

Neurodevelopment relies on the precise coordination of cellular processes that determine the fate of multipotent *PAX6*-expressing radial glial cells (RGCs)[1–3]. RGCs are the major neural stem cells (NSCs) that give rise to glia and neurons in the human cortex[4,5]. The fate of these NSCs relies on their ability to undergo symmetric or asymmetric division, a process that ultimately determines whether they self-renew or differentiate into specialized cell types[4,5]. NSCs give rise to intermediate progenitor cells (IPCs)[6,7], which are *EOMES* (TBR2)-expressing[8,9] cortex-specific transit amplifying cells[10] committed to producing glutamatergic projection neurons of cortical layers two through six[11,12]. Given the high bioenergetic demands and metabolic complexity of NSCs, disruption of mitochondrial morphology and function can impair critical stem cell transitions during neurogenesis[13–15]. Despite this, the precise role of mitochondrial morphology and function in these intricate transition states is incompletely understood.

Myeloid cell leukemia-1 (MCL-1) is a mitochondrial membrane protein identified as a regulator of mitochondrial morphology through mechanisms that are independent of its canonical anti-apoptotic function[16–20]. Initially recognized only as a member of the B-cell lymphoma 2 (BCL-2) family for its BCL-2 homology-3 (BH3) domain and role in preventing cell death at the outer mitochondrial membrane (OMM)[21], MCL-1 has been well-established to have non-apoptotic functions[17,18,22–26]. Disruption of MCL-1 causes mitochondrial dysfunction in human cardiomyocytes[20,23], as well as improper development of hematopoietic stem cells[27], B cell and T cell progenitors[28], activated B cells[29], and the central nervous system[30]. MCL-1 has also been found to localize to the inner mitochondrial membrane (IMM), where it may interact with cristae-shaping proteins, such as optic atrophy type 1 (OPA1)[18,19,23]. However, the function of MCL-1 at the IMM remains poorly delineated. Inhibition of MCL-1 has been explored as a promising treatment for chemo-resistant tumors but has not advance beyond Phase I/II in clinical trials due

65 to potential cardiotoxicity. Inhibition of MCL-1 with existing small molecule inhibitors results in
66 impaired cardiomyocyte function and disruption of mitochondrial morphology[31], but more
67 investigation is needed to determine whether this applies to other bioenergetically demanding cell
68 types. Like cardiomyocytes, NSCs are bioenergetically demanding cells; however, the effects of
69 MCL-1 pharmacological inhibition on human NSCs (hNSCs) remain unknown.
70
71 Previous work has reported a close association between MCL-1, mitochondrial morphology, and
72 pluripotent stem cell identity of human embryonic stem cells (hESCs)[17]. Knockdown of *MCL-1*
73 (*MCL-1*^{KD}) in hESCs[17] results in an elongated mitochondrial network, a phenotype linked to
74 differentiation[32]. Moreover, *MCL-1*^{KD} hESCs exhibited loss of key pluripotent transcription factors
75 and identity markers, including *OCT4* and *NANOG*[33,34]. Other studies have established a
76 postmitotic period of fate plasticity, controlled by mitochondrial morphology, during mouse brain
77 development[35,36]. When mitochondria remain elongated (low fission), NSCs divide symmetrically,
78 thus expanding the pool of progenitor cells. Conversely, if fission increases, this drives NSCs
79 toward differentiation[35,36]. *In vivo* mouse studies highlight the importance of MCL-1 in mouse
80 embryonic survival and proper fetal neurodevelopment[26]. A gene swap approach in which the
81 coding sequence of the *Mcl-1* gene was replaced with other anti-apoptotic genes, *BCL-2* (*Mcl-*
82 *1*$^{BCL-2}$), *BCL-XL* (*Mcl-1*$^{Bcl-xL}$), or *A1* (*Mcl-1*^{A1}), resulted in neurodevelopmental defects that could
83 not be rescued by anti-apoptotic functions alone, providing evidence that the noncanonical
84 functions of MCL-1 are indispensable for proper neurodevelopment[26]. Studies in the field have
85 shown that disruption of the fatty acid oxidation (FAO) pathway promotes asymmetric
86 differentiation of adult mouse NSCs, highlighting the role of FAO in regulating NSC fate
87 decisions[37–40].
88
89 Work from the Opferman and Walensky groups revealed an unexpected link between MCL-1
90 and FAO in cancer cells[22,24,25]. Inhibition of MCL-1 results in decreased oxidation of long-chain

91 fatty acids (LCFAs) in cancer cells[22,24], likely due to the disrupted interaction between MCL-1
92 and the BH3-like domain of acyl-CoA synthetase long-chain family member 1 (ACSL-1). This
93 suggests that MCL-1 is a direct modulator of FAO in cancer cells[25]; however, this has not been
94 mechanistically investigated in the context of human neurodevelopment.
95
96 FAO is a metabolic process critical for energy production and cellular homeostasis that occurs
97 within the mitochondrial matrix and requires LCFAs to pass the OMM and IMM. Starting at the
98 OMM, LCFAs are first activated to acyl-CoA derivatives by ACSL1 and then catalyzed by carnitine
99 palmitoyltransferase I (CPT1) into a fatty acylcarnitine. At the IMM, carnitine palmitoyltransferase
100 II (CPT2) functions to cleave the fatty acylcarnitine and catalyze the fatty acid back to fatty acyl-
101 CoA for β-oxidation by Very Long Acyl-CoA Dehydrogenase (VLCAD) at the matrix. The
102 enzymatic breakdown of LCFAs is a multistep process that produces acetyl-CoA, a metabolic
103 byproduct which enters the tricarboxylic acid (TCA) cycle where it generates citrate that exits
104 the mitochondria and can be used for histone acetylation[41,42]. Disruption of the FAO pathway
105 promotes asymmetric differentiation of pluripotent and neural stem cells, suggesting a role of
106 FAO in stem cell fate decisions[37–40,43]. Although FAO modulates neurodevelopment and MCL-
107 1 is known to play a role in cancer cell FAO, the role of MCL-1 in FAO during human
108 neurodevelopment has not been explored. Here, we report the non-apoptotic effects of MCL-1
109 inhibition on mitochondrial and cristae morphology and FAO in hNSCs. Our findings provide
110 evidence that MCL-1 maintains the integrity of mitochondrial cristae and neural progenitor cell
111 identity.
112
113

Results

MCL-1 inhibition disrupts mitochondrial architecture and inner membrane organization in human neural stem cells

MCL-1 is known for its canonical function as an anti-apoptotic member of the BCL-2 family and is indispensable for the survival of human induced pluripotent stem cells[17], hematopoietic stem cells[27,44], and cardiomyocytes[23]. Similarly, embryonic neural precursor cells depend on MCL-1, as conditional knockout murine models display widespread apoptosis upon MCL-1 loss[45]. These findings suggest a general dependency on MCL-1 for the survival of neural precursor cells across developmental stages. To examine the effect of MCL-1 inhibition on hNSCs, we differentiated hESCs with SMAD inhibitors, as previously described[46], and treated them with S63845, a selective BH3 mimetic inhibitor of MCL-1, for 24 or 48 hours (**Figure 1A**).

Previous studies reported an increase in MCL-1 protein levels upon MCL-1 inhibition, which is speculated to be due to the stabilization of MCL-1 whereby MCL-1 is protected from degradation by proteases when its BH3 domain is occupied[47]. Using RT-qPCR, we observed a downregulation of *MCL-1* at 24 hours of inhibition but not 48 hours (**Supplementary Figure 1A**). Co-treatment with Q-VD-OPh (QVD), a potent pan-caspase inhibitor, did not result in downregulation of *MCL-1* expression (**Supplementary Figure 1B**). As previously reported, we also observed an increase in MCL-1 protein levels in hNSCs at both timepoints (**Supplementary Figures 1C-D**) despite the downregulation of *MCL-1* expression at 24 hours. This increase in MCL-1 protein levels serves as an internal control that the S63845 small molecule inhibitor is effectively inhibiting MCL-1 in hNSCs. However, this upregulation was not observed when hNSCs were co-treated with QVD (**Supplementary Figures 1E-F**).

138 The mitochondrial network of hNSCs treated with S63845 at both timepoints exhibited a swollen
139 mitochondrial network with greater volume and surface area as revealed by super-resolution
140 microscopy (**Figure 1B**). MCL-1 inhibition at 48 hours resulted in a significant reduction in
141 mitochondrial content. The maximum mitochondrial volume and equatorial diameter revealed an
142 expanded mitochondrial network at both timepoints (**Supplementary Figure 2A**). hNSCs co-
143 treated with QVD do not exhibit these mitochondrial network changes (**Supplementary Figure**
144 **2B**).
145
146 Due to the critical role of mitochondrial cristae in metabolism regulation, we interrogated whether
147 the effects of MCL-1 inhibition on mitochondrial morphology extended to the ultrastructure of the
148 cristae using transmission electron microscopy (TEM) (**Figure 2A**). The hNSCs treated with MCL-
149 1 inhibitor exhibited an atypical cristae morphology at 48 hours (**Figure 2B**). Three-dimensional
150 reconstruction of focused ion beam-scanning electron microscopy (FIB-SEM) images further
151 revealed an increase in cristae volume and surface area (**Figures 2C-D**) but not mitochondrial
152 branching index (MBI) or sphericity (**Supplementary Figure 3A**). MCL-1 inhibition led to
153 extensive loss of cristae organization in S63845-treated cells (**Figure 2A–E**). Compared to the
154 densely folded membranes of control mitochondria, those from MCL-1–inhibited cells exhibited
155 swollen matrices and sparse, disordered cristae. Volumetric analyses revealed a sharp increase
156 in both cristae surface area and volume, underscoring the significance of MCL-1 for maintaining
157 inner membrane complexity and structural integrity.
158
159 **MCL-1 activity preserves OPA1 proteostasis and MICOS complex stability**
160 Given the pronounced inner membrane defects, we examined the proteins responsible for cristae
161 shaping and junction formation (**Figure 3A**). The cristae structure is maintained by the
162 mitochondrial contact site and cristae-organizing system (MICOS) complex, composed of the
163 MIC60 subcomplex (MIC60, MIC19, MIC25) and the MIC10 subcomplex (MIC10, MIC26, MIC27)

164 bridged together by MIC13/QIL[48]. The MICOS complex is responsible for establishing junctions
165 that are required for cristae biogenesis in the IMM to increase its surface area for synthesis of
166 adenosine triphosphate (ATP) via oxidative phosphorylation through the electron transport
167 chain[16,49]. The large GTPase, OPA1, contributes to the stabilization of the MICOS and cristae
168 architecture[50]. The long form of OPA1 (OPA1-L) has a well-established role in IMM fusion[51] and
169 is also critical for the maintenance of cristae lumen width[52]. Cooperatively, the short forms of
170 OPA1 (OPA1-S1/2) maintains the length of the cristae lumen[52]. We first examined whether MCL-
171 1 inhibition alone or in combination with QVD alters the expression of *MIC60* or *OPA1* mRNA and
172 found no significant fold change (**Figure 3B-D**). We detected a decrease of OPA1-S1 protein
173 levels at 24 and 48 hours and of OPA1-S2 at 48 hours of MCL-1 plus caspase inhibition, but not
174 with MCL-1 inhibition alone (**Figures 3C-E**). Thus, MCL-1 inhibition disrupts the balance between
175 long (fusion-competent) and short OPA1 isoforms, hindering proteolytic cleavage of OPA1-L into
176 smaller fragments. Immunoblotting analysis for MIC60 and MIC10, the core components of the
177 MICOS subcomplexes, revealed a similar reduction in abundance of MIC10 protein levels at 48
178 hours of MCL-1 inhibition (**Figure 3C**). Co-treatment with the caspase inhibitor QVD did not
179 rescue the levels of MIC10 (**Figure 3E**), indicating that OPA1 processing and MICOS
180 destabilization are not a consequence of caspase activation. We did not observe a change in
181 other MICOS protein levels (**Figure 3C and Supplementary Figure 3B**). These data identify
182 MCL-1 as a critical regulator of mitochondrial inner membrane organization, acting upstream of
183 OPA1- and MICOS-dependent cristae maintenance.
184

185 **MCL-1 inhibition impairs FAO and metabolic coupling**

186 We predict that the FAO transmembrane enzymes and transport proteins heavily rely on the
187 proper assembly and structure of the OMM and IMM (**Figure 4A**). Previous investigations have
188 shown a close interaction between MCL-1 and FAO enzymes in cancer cells[22,25], and mouse
189 studies have also established the importance of FAO for maintenance of embryonic

190 neurodevelopment and adult NSCs[26,38,43]. To explore whether the mitochondrial structural
191 perturbations extend to mitochondrial function, we assessed key regulators of fatty acid β-
192 oxidation. Expression analyses revealed no changes in FAO enzyme transcripts with MCL-1
193 inhibition alone (**Figure 4B**), but a significant downregulation of *CPT2* transcripts at 24 hours
194 following MCL-1 and caspase inhibition, while *ACSL1* and *CPT1a* expression remained stable
195 (**Figure 4C**). Increased protein levels of CPT1a were detected at 48 hours following inhibition of
196 MCL-1 (**Figure 4D**). Furthermore, co-treatment with caspase inhibition revealed an increase of
197 CPT1a levels earlier at 24 hours, along with a decrease of CTP2 at 48 hours and VLCAD at both
198 timepoints (**Figure 4E**). The alteration in β-oxidation components persisted despite caspase
199 inhibition, confirming a direct metabolic effect of MCL-1 loss. These findings suggest that MCL-1
200 supports mitochondrial lipid utilization by sustaining the expression of enzymes critical for fatty
201 acid transport and oxidation.
202
203 Fatty acids get stored in lipid droplet organelles when they are not utilized for β-oxidation.
204 Accumulation of lipid droplets upon MCL-1 inhibition was previously reported in cancer cells and
205 murine liver as a marker of fatty acid β-oxidation disruption[25]. To further investigate the impact of
206 MCL-1 inhibition on FAO, hNSCs were cultured in nutrient-deficient DMEM media supplemented
207 only with palmitate during treatment with MCL-1 inhibitor, followed by a 2-hour starvation period
208 in HBSS and S63845 (**Figure 5A**). Consistent with impaired β-oxidation, S63845-treated hNSCs
209 accumulated excess neutral lipids when challenged with palmitate as their only resource for fuel
210 (**Figure 5B**). Quantitative imaging revealed increased the average and maximum volume of lipid
211 droplets (**Figure 5C**), indicative of reduced lipid turnover and a shift toward storage. These data
212 suggest that MCL-1 sustains metabolic flux as fatty acids fail to import to the matrix and
213 accumulate in lipid droplets.
214
215 **MCL-1 maintains neural progenitor identity and supports neuronal differentiation**

216 Given the role of MCL-1 in FAO and the mitochondrial and metabolic perturbations triggered by
217 MCL-1 inhibition, we investigated the effects of S63845 treatment on neurogenic progression.
218 Although we did not detect changes in global protein levels of hNSC identity markers
219 (**Supplementary Figure 4A**), we observed a significant downregulation of *PAX6* (a marker of
220 neural stem cell identity) and *EOMES* (the gene encoding TBR2, a marker of IPCs) at 24 hours
221 that was not rescued by QVD co-treatment and persisted into 48 hours with co-treatment
222 (**Supplementary Figure 4B)**. Immunofluorescent imaging revealed a small population of IPCs
223 ($PAX6^-/TBR2^+$) in the culture of hESCs induced with dual SMAD inhibition. IPCs are committed
224 progenitor cells that give rise to glutamatergic projection neurons. MCL-1 inhibition selectively
225 reduced the proportion of $PAX6^-/TBR2^+$ IPCs while sparing $PAX6^+$ RGC-like progenitors (**Figure**
226 **6A**). This loss of IPCs persisted under caspase inhibition (**Figure 6B**), suggesting that MCL-1 is
227 critical for maintaining the identity of this progenitor pool through non-apoptotic mechanisms. To
228 determine how these effects on IPCs impact neuronal differentiation, we first examined the ability
229 of the cells to proliferate using EdU labeling and found no significant changes in late or early S-
230 phase (**Supplementary Figure 5A&B**). To further investigate the potency of neural
231 stem/progenitor cells, we examined their ability to differentiate and give rise to newborn neurons
232 using βIII-tubulin staining (**Figure 7**). Control cells formed dense neurite networks with extensive
233 βIII-tubulin labeling, whereas MCL-1–inhibited neurons displayed sparse and truncated
234 processes, reflecting defective neurite extension and maturation (**Figure 7**). When treated with
235 MCL-1 inhibitor, neural stem/progenitor cells gave rise to less newborn neurons; however, this
236 phenotype was rescued upon co-treatment with QVD. This sheds light on the importance of MCL-
237 1 for the potency of neural stem/progenitor cells to undergo proper differentiation and for newborn
238 neurons to undergo proper maturation (**Figure 7B**). The absence of overt cytotoxicity suggests
239 that MCL-1 directly supports neuronal commitment rather than survival alone.
240

241 **Discussion**

242 Although MCL-1 has been traditionally studied as an anti-apoptotic BCL-2 family member[21,53],
243 accumulating evidence supports its critical role in maintaining mitochondrial homeostasis across
244 diverse cell types[25,26]. Our findings extend this paradigm to the developing human brain. By
245 combining ultrastructural, molecular, and functional analyses, we report that MCL-1 sustains the
246 integrity of mitochondrial architecture and its functional coupling to metabolic flux. Inhibition of
247 MCL-1 leads to structural collapse of the cristae and disassembly of the MICOS complex as well
248 as OPA1, two scaffolds required for cristae maintenance. Consequently, MCL-1 inhibition impairs
249 FAO metabolism, as evidenced by altered FAO enzyme levels and lipid droplet accumulation. We
250 propose that efficient FAO depends on both cristae surface area and the localization of β-
251 oxidation enzymes to defined subdomains of the inner membrane. These perturbations are
252 accompanied by defects in IPC maintenance and neuronal maturation. Our findings establish a
253 non-apoptotic role for MCL-1 in sustaining mitochondrial organization and metabolic competence,
254 which are indispensable for proper human neurogenesis. Taken together, the data suggest that
255 MCL-1 integrates mitochondrial architecture with metabolic capacity to support progenitor identity.
256

257 While MCL-1 has been reported to influence FAO in cancer cells and to localize to the IMM, its
258 impact on cristae integrity has remained unexplored until now. Our findings bridge this gap by
259 revealing that MCL-1 is necessary for maintaining cristae organization and metabolic FAO
260 competence in hNSCs. The observed reduction in mitochondrial content upon MCL-1 inhibition
261 likely reflects a compensatory failure where mitochondria are increased in volume and surface
262 but lose metabolic function as apparent by lipid droplet accumulation. We find this disruption to
263 be coupled to a decline in FAO enzymes. Further investigation is required to determine whether
264 ACSL1 localization is affected by MCL inhibition in hNSCs, as reported in cancer cells. Whether
265 ACSL1 integrates into the OMM or needs only to be in close proximity to the OMM for the

activation of LCFAs is not known. Given that the altered FAO enzyme levels were all downstream of ACSL1, this raises the question of whether ACSL1 is a rate-limiting step in the mitochondrial beta-oxidation pathway. If ACSL1 is displaced from the mitochondria, this may disrupt a feedback loop that maintains the expression and stabilization of FAO enzymes, thereby dismantling the FAO signaling pathway and leading to lipid oxidation dysfunction. The alterations in FAO enzyme expression and protein levels accompanied by mitochondrial swelling suggest that MCL-1 coordinates spatial coupling between lipid activation and oxidative metabolism.

Given that efficient FAO is a defining feature of the progenitor metabolic state, this association could represent a key mechanism linking mitochondrial structure and function to the maintenance of stem cell fate. The influence of mitochondrial function on developmental fate decisions is increasingly recognized. *In vivo* and *in vitro* studies have identified a postmitotic window of neurogenic plasticity directed by mitochondrial morphology[45,36,54]. Moreover, disruption of the FAO pathway promotes asymmetric differentiation of adult mouse pluripotent and neural stem cells, signifying a role of FAO in stem cell fate decisions[38,43]. Our data reveal that MCL-1 inhibition disrupts this balance. MCL-1 inhibition does not alter hNSC proliferation but instead results in reduced intermediate progenitors and impaired neuronal differentiation and maturation. Bioenergetically demanding cells must meet their metabolic needs for proper function and survival. The metabolic intermediates of mitochondrial FAO, such as acetyl-CoA, may alter gene expression via histone modifications (e.g., acetylation) and ultimately influence cell fate decisions. In the delicate process of development, high-energy-demanding cells must maintain a specific metabolic profile for survival, making metabolism a quality-control checkpoint. If a cell does not meet the criteria for differentiation, its fate shifts to maintain tissue integrity.

A key question emerging from this study is whether MCL-1 directly regulates FAO through physical association with lipid import enzymes or indirectly by maintaining cristae topology. We

292 hypothesize that MCL-1 associates with both MICOS and FAO enzymes at discrete cristae
293 contact points, thereby coupling membrane morphology to metabolic signaling.
294
295 Taken together, our results position MCL-1 upstream of the structural regulators OPA1 and
296 MICOS and define a previously unappreciated dimension of MCL-1 function in human
297 neurogenesis, albeit using an *in vitro* experimental paradigm. Beyond its canonical anti-apoptotic
298 role, MCL-1 emerges as a structural and metabolic hub that links cristae architecture, lipid
299 oxidation, and lineage progression. We propose a model in which MCL-1 associates with MICOS
300 and FAO complexes to maintain cristae organization and metabolic flux, thereby sustaining the
301 progenitor state and enabling efficient neuronal differentiation. Future studies dissecting the
302 molecular interfaces between MCL-1, MICOS proteins, and FAO enzymes will be critical for
303 determining whether MCL-1 acts as a scaffold that integrates mitochondrial structure and
304 metabolic signaling. In alignment with our observations, mutations in cristae-shaping proteins are
305 associated with severe neurodevelopmental disorders, reinforcing the notion that mitochondrial
306 ultrastructure steers fate specification. Understanding this connection could illuminate
307 fundamental mechanisms by which mitochondrial morphology and function influences stem cell
308 potency during neurodevelopment.

309 **Methods**

310 **Human Embryonic Stem Cells (hESCs)**

311 Human embryonic stem cell line, H9 (WA09), was obtained from WiCell Research Institute
312 (Wisconsin). H9s were maintained in mTeSR (STEMCELL Technologies, cat # 85850) media on
313 6-well plates coated with Matrigel (Corning, cat # 354277) at 37°C with 5% CO2. Culture medium
314 was changed daily. Cells were checked daily for differentiation and were passaged every 3-4 days
315 using Gentle cell dissociation solution (STEMCELL Technologies, cat # 07174). All experiments
316 were performed under the supervision of the Vanderbilt Institutional Human Pluripotent Cell
317 Research Oversight (VIHPCRO) Committee. Cells were periodically checked for contamination.

318

319 **hESC-derived hNSC culture**

320 H9s were cultured until reaching 70-80% confluency, ensuring minimal differentiation at the
321 colony edges. Cells were dissociated using 1 mL of a Gentle Cell Dissociation Reagent
322 (STEMCELL Technologies, cat # 100-0485) and incubated at 37°C for 8 minutes. 2 mL of DMEM-
323 F12 (Thermo Scientific, cat # 11320033) supplemented with 10 μM of ROCK inhibitor
324 (STEMCELL Technologies, cat # 72307) was added to each well. Cells were gently scraped,
325 pipetted for transfer into a conical tube, and centrifuged at 300 x g for 5 minutes. Cell pellet was
326 resuspended in STEMdiff™ SMADi Neural Induction Medium (NIM) (STEMCELL Technologies,
327 cat # 08581) supplemented with 10 uM ROCK inhibitor. Cell suspension was counted and plated
328 at a density of 2.0-2.5x10^6 cells per well in a 6-well plate. Cells were incubated at 37°C for 7 days,
329 with daily feeding of NIM.

330

331 **Western blot**

332 Cells were harvested in lysis buffer containing 1% Triton X-100 (Sigma, cat # T9284), 1X complete
333 protease inhibitor cocktail (Roche, cat # 04693159001), 1X PhosSTOP phosphatase inhibitor

334 (Roche, cat # 04906837001), and 0.5mM PMSF (RPI, cat # P20270). Samples were kept on ice
335 and vortexed for 30 seconds every 10 minutes. Lysates were centrifuged at 14,100 x g for 30
336 minutes at 4ºC. Supernatant was collected and protein concentrations were quantified using the
337 Pierce BCA Protein Assay Kit (ThermoScientific, cat # 23225). Western blotting was performed
338 using the Bio-Rad Mini-PROTEAN Electrophoresis System (Bio-Rad, cat # 1658036). Samples
339 were run on 4-20% Mini-PROTEAN TGX gels (Bio-Rad, cat # 4561095). Protein was transferred
340 from gels onto methanol activated PVDF membranes (Bio-Rad, cat # 1620177). All membranes
341 were washed in Tris-buffered saline with 0.1% Tween-20 (TBST) and blocked in TBST containing
342 5% milk for 1 hour at room temperature. Primary antibodies were incubated at listed dilution in
343 TBST containing 5% milk overnight at 4ºC. Secondary antibodies were used at listed dilution in
344 TBST containing 5% milk and incubated for 1 hour at room temperature. Protein signal was
345 developed using either Pierce ECL Western Blot Substrate (32109, ThermoScientific) or
346 SuperSignal West Femto (34094, ThermoScientific), depending on the sensitivity of the primary
347 antibody. Protein signal was visualized using the Amersham Imager 600 (29-0834-61, GE Life
348 Sciences). Acquired images were quantified using Thermo Fisher Scientific iBright Analysis
349 Software and representative images were composed using Affinity Designer 2.
350

Antibody	Source	Catalogue Number	RRID	Dilution	Application
Mouse anti-mitochondria	Abcam	ab92824	AB_10562769	1:200	Immunofluorescence
Mouse anti-PAX6	BD Pharmingen	561462	AB_10715442	1:200	Immunofluorescence
Rabbit anti-EMOES (TBR2)	Cell Signaling Technology	81493	AB_2799974	1:200	Immunofluorescence
Mouse anti-b-Actin	Sigma-Aldrich	A1978	N/A	1:10,000	Western blot
Rabbit anti-cleaved PARP	Cell Signaling Technology	5625S	AB_10699459	1:1000	Western blot
Rabbit anti-MCL-1	Cell Signaling Technology	94296S	AB_2722740	1:1000	Western blot

Rabbit anti-CHCHD3 (MIC19)	Proteintech	25625-1-AP	AB_2687533	1:10,000	Western blot
Rabbit anti-IMMT (MIC60)	Sigma-Aldrich	HPA036164	AB_2674979	1:5000	Western blot
Rabbit anti-OPA-1	Cell Signaling Technology	67589S	AB_2799728	1:5000	Western blot
Rabbit anti-PAX6	Cell Signaling Technology	60433S	AB_2797599	1:500	Western blot
Mouse anti-SOX2	Abcam	ab79351	AB_10710406	1:500	Western blot

RNA extraction and cDNA synthesis

Cells were collected in 1000 µl TRIzol reagent. 200 µl of chloroform was added and the samples were incubated at room temperature for 5 minutes prior to centrifugation at 12,000 x g at 4°C. The aqueous phase was collected and 500 µl of isopropanol was added to precipitate RNA. Samples were incubated for 25 minutes at room temperature, followed by centrifugation at 12,000 x g for 10 minutes at 4°C. The RNA pellet was washed with 75% ethanol, semi-dried, and resuspended in 30 µl of DEPC-treated water. Concentration was measured and 2 µg per sample was treated with DNAse (New England Biolabs #M0303) prior to generating cDNA using the manufacturer's protocol (Thermo Fisher #4368814).

Quantitative PCR (RT-qPCR)

50 ng of cDNA sample was used to run RT-qPCR using 20 µM of the primers listed in the table. QuantStudio 3 Real-Time PCR machine, SYBR green master mix (Thermo Fisher #4364346), and manufacturer instructions were used to set up the assay.

Target	Forward Primer	Reverse Primer
GAPDH	ACAACTTTGGTATCGTGGAAGG	GCCATCACGCCACAGTTTC
GPI	GTGTACCTTCTAGTCCCGCC	GGTCAAGCTGAAGTGGTTGAAGC
MCL-1	GTGCCTTTGTGGCTAAACACT	AGTCCCGTTTTGTCCTTACGA

MIC19	GAGGCGGACGAGAATGAGAAC	ACCAGAATACCGCTGAGACTTC
MIC60	CGATTCAGTCGGGTCCACTAA	AGCTGGAGTATCTCCCTTTTGT
OPA1	TGTGAGGTCTGCCAGTCTTTA	TGTCCTTAATTGGGGTCGTTG
PAX6	TGGGCAGGTATTACGAGACTG	ACTCCCGCTTATACTGGGCTA
SOX2	CCATGCAGGTTGACACCGTTG	TCGGCAGACTGATTCAAATAATACAG
TBR2	GTGCCCACGTCTACCTGTG	CCTGCCCTGTTTCGTAATGAT

366

367 **Immunofluorescence**

368 Cells were plated on 35 mm glass-bottom dishes (glass thickness of 0.16-0.19 mm) for confocal
369 spinning disk immunofluorescence. Cells were fixed with 4% paraformaldehyde for 20 min and
370 permeabilized in 1% Triton-X-100 for 10 min at room temperature. After blocking in 10% BSA for
371 1 hour, cells were treated with primary and secondary antibodies using standard methods.
372 Primary antibodies were incubated at listed dilution in 10% BSA overnight at 4ºC. Secondary
373 antibodies were used at listed dilution in 10% BSA and incubated for 1 hour at room temperature.
374 The nuclear stain used was HOECHST (Thermo Scientific, cat # H3570) and cells were mounted
375 in Fluoromount-G (Electron Microscopy Sciences #17984-25) prior to imaging. Cells were labeled
376 for EdU using the manufacturer's protocol (Thermo Fisher #C10340). Lipid droplet staining was
377 done live using BODIPY (Cayman Chemical Company #25892). Cells were incubated at 37ºC for
378 15 minutes in 4 μM BODIPY prior to fixation in 4% PFA.

379

380 **Spinning Disk Confocal image acquisition**

381 Images were acquired using a Nikon Spinning Disk Confocal outfitted with a Yokogawa CSU-X1
382 spinning disk head, Andor DU-897 EMCCD camera, and high-speed piezo [z] stage. All 100X
383 images were acquired with a step size of 0.2 μm, while 20X images were acquired with a step
384 size of 2 μm. Image processing and quantification was performed using NIS Elements (Nikon)
385 and all representative images were generated using Fiji.

386 For mitochondrial morphology, we segmented mitochondria in 3D and performed skeletonization
387 of the resulting 3D mask. Skeleton major axis length, volume, and surface area measurements
388 were exported into GraphPad Prism v9.
389
390 **Tissue Preparation for TEM and FIB-SEM**
391 Neural progenitor cells were plated at $1.5x10^6$ cells per 35 mm dish on Matrigel. The cells were
392 washed with 1X PBS (3X), fixed in 2.5% glutaraldehyde in 0.1 M cacodylate prewarmed to 37ºC,
393 left to cool down at room temperature for 1hr, and placed at 4ºC for an additional 24-48 hour of
394 fixation. Cells were washed from fixative with 1X PBS (3x). Samples were sequentially post-fixed
395 using the OTO method: 1.5% potassium ferrocyanide, 1% OsO4 in 0.1 M cacodylate for 30
396 minutes on ice, then 1% thiocarbohydrazide for 10 minutes, followed by 1% OsO4 in ddH2O for
397 10 minutes. Samples are then enblock stained with 2% uranyl acetate followed by lead aspartate.
398 The samples were then dehydrated in a graded ethanol series and infiltrated with Durcupan resin
399 using acetone as the transition solvent. The resin was polymerized at 60ºC for 48 hours. For TEM,
400 sections were cut on a Leica UC7 at a nominal thickness of 50 nm with no post-section staining.
401 For FIB-SEM, samples were prepared as previously described[55].
402
403 **TEM image acquisition and Cristae Scoring**
404 Sections were imaged with either a ThermoFisher Scientific Tecnai T12 operating at 100 keV
405 using an AMT nanosprint5 CMOS camera or a JEOL 2100+ operating at 200 keV using an AMT
406 nanosprint15 II CMOS camera. In both cases, AMT acquisition software was used for imaging.
407 The TEM images were analyzed using cristae scoring (Lam et. Al, 2021)[56]. The files were first
408 renamed to blind the scoring process. The images were then blindly scored. A score was provided
409 for each mitochondrion based on the quality of the cristae. The scoring rubric was as follows: 0 -
410 there were no crista, 1 - more than 50% of the mitochondrial area did not have cristae, 2 - more

411 than 25% of the mitochondria was without cristae, 3 - lots of cristae but irregular in structure, and
412 4 - many cristae that are regular structures.
413
414 **FIB-SEM image acquisition**
415 Sections were imaged with Zeiss Crossbeam 550 FIB-SEM using ATLAS5 software for
416 automated volumetric acquisition. Sample blocked were polished with a diamond knife and coated
417 with platinum. Platinum pads were deposited via GIS on ROIs of interest, followed by milling in
418 tracking marks and coating with GIS carbon. Milling was performed using a 700 pA Ga beam at
419 8 nm slice depth, imaging was performed 1.5 keV electron beam using the in column ESB detector
420 for imaging at 8 nm pixels to make isotropic voxels. Volumetric slice alignments were performed
421 in ATLAS5 using the two-window alignment method.
422
423 **FIB-SEM mitochondrial image analysis**
424 FIB-SEM stacks were first cropped using Fiji is just Image J (FIJI). In the FIB-SEM stacks, none
425 of the cells imaged were able to be visualized completely. Therefore, the crop size and location
426 were selected by choosing a cell with bright, visible mitochondria. The crop was 500 x 500 pixels
427 with a 3,000 nm depth. The cropped image was then imported into the FIJI LabKit plugin for
428 segmentation[57]. For segmentation, each mitochondrion was manually traced with a separate label
429 ID. Quality control was then performed following each mitochondrion through the entirety of the
430 Z-stack and tracking all locations where the membranes connect. Any mitochondria that merged
431 in any of the frames were labeled with the same label ID. The cropped FIB-SEM image and the
432 proofread segmentation masks were imported into the IMARIS software. Ortho slices in the XY
433 and XZ planes were added, and the proofread mask was selected to be identified by ID. This
434 identifies each separate mitochondrion. Any mitochondria that were still split were manually
435 combined in the IMARIS software using the unify feature. A clipping plane was then added.
436 Animations were made using the animations tab in IMARIS with 50 frames per second and 1,000

437 frames total. Still images were captured using the screenshot feature. Volume quantification was
438 done by volume measurement provided in the statistics tab in IMARIS. Surface area quantification
439 was manually calculating using volume and sphericity measurements from the IMARIS statistics
440 tab using the equation: $\frac{\pi^{\frac{1}{3}}(6*Volume)^{\frac{2}{3}}}{Sphericity}$. Lastly, the mitochondrial branching index (MBI), was
441 calculated by obtaining the BoundingBox00 length A (longest side) and BoundingBox00 length C
442 (Shortest side) in the Vantage 2D tab and then dividing Length C/ Length A manually[58].
443
444 **FIB-SEM cristae image analysis**
445 The same FIB-SEM cropped images were used for the segmentation of the cristae. The cropped
446 images were imported into FIJI and applied Contrast Limited Adaptive Histogram Equalization
447 (CLAHE) to increase contrast. They were then imported into the LabKit plugin for segmentation.
448 Each crista was manually traced, and all the cristae within one mitochondrion were labeled with
449 the same label ID. Quality control was then performed, ensuring each mitochondrion had all its
450 cristae labeled with the same ID. The cropped FIB-SEM image and the proofread segmentation
451 masks were imported into the IMARIS software. Ortho slices in the XY and XZ planes were added,
452 and the proofread mask was selected by ID. This identifies each separate mitochondrion's cristae.
453 Any errors in the cristae mask were merged using the unify feature in IMARIS. A clipping plane
454 was then added to show the mitochondria throughout the entire z-plane. Animations were made
455 using the animations tab in IMARIS with 50 frames per second and with 1,000 frames total. Still
456 images were taken using the snapshot feature. Volume quantification was done by volume
457 measurement provided in the statistics tab in IMARIS. Surface Area quantification was manually
458 calculated using volume and sphericity measurements from IMARIS statistics tab using the
459 equation: $\frac{\pi^{\frac{1}{3}}(6*Volume)^{\frac{2}{3}}}{Sphericity}$. Cristae measurements were then normalized to the corresponding
460 mitochondria by dividing the crista measurement by the mitochondrion measurement (i.e.,

$\frac{Crista\ Volume}{Mitochonrion\ Volume}$. The mitochondria segmentation was then added to the same IMARIS file as a second surface. The label was chosen by ID, and the surface type was changed to transparent to show the cristae within those mitochondria. Images were taken using the snapshot function, and animations were made with 50 frames per second and 1,000 frames total.

Statistical analysis

All experiments were performed with at least 3 biological replicates. Statistical significance was determined by one-way, repeated measures one-way ANOVA, or t-test as appropriate for each experiment. Significance was assessed using Fisher's protected least significance difference test. GraphPad Prism v9 was used for all statistical analysis and data visualization. Error bars in all bar graphs represent the standard error of the mean unless otherwise noted in the figure. No outliers were removed from the analyses. For all statistical analyses, a significant difference was accepted when $P < 0.05$.

Figure Legends

Figure 1. S63845 impacts mitochondrial content and morphology.

(A) Schematic detailing the neural induction of human embryonic stem cells (hESCs) using SMAD inhibition (SMADi) for the derivation of the human neural stem cells (hNSCs) tissue culture model. hNSCs are maintained in neural induction media (NIM) with daily media changes until they are passaged on day 7. hNSCs are given a 24-hour acclimation period on day 8 before treatment on day 9 with 1μm S63845 (MCL-1 inhibitor), and DMSO as the control group. Samples were then collected at 24- and 48-hours post-treatment on days 10 and 11 after which cells were fixed and stained for imaging on a SoRa spinning disk confocal (SDC) microscope. (B) Immunofluorescent images of mitochondria (anti-mito in magenta) and nuclei (Hoechst in cyan) acquired on SoRA SDC at 100X (scale bar = 40μm). Representative images (n=3) of 24- and 48-hours post-treatment with DMSO control and S63845 (MCL-1 inhibitor). Quantification of mitochondrial content and average measures of mitochondrial morphology. Nine images were acquired per condition and plotted in gray. Each large, open-shape data point represents the mean per biological replicate. Shape of data point corresponds to each biological replicate (open circle for n=1, open square for n=2, and open triangle for n=3). Means of the biological replicates were analyzed using a parametric two-tailed unpaired t-test with a Welch's Correction. Error bars represent standard error of the mean.

Figure 2. MCL-1 inhibition compromises mitochondrial cristae integrity.

(A) Schematic detailing the neural induction of human embryonic stem cells (hESCs) using SMAD inhibition (SMADi) for the derivation of the human neural stem cells (hNSCs) tissue culture model. hNSCs are maintained in neural induction media (NIM) with daily media changes until they are passaged on day 7. hNSCs are given a 24-hour acclimation period on day 8 before treatment on day 9 with 1μm MCL-1 inhibitor (S63845 MCL-1i) with DMSO as the control group. Samples were then collected at 48-hours post-treatment on day 11 after which cells were fixed and processed

505 for transmission electron microscopy (TEM) or focused ion beam-scanning electron microscopy
506 (FIB-SEM). (B) Representative TEM images (n=3) of hNSC mitochondrial cristae 48-hours post-
507 treatment with DMSO control and S63845 MCL-1 inhibitor. Scale bar = 600nm. (C) 3-dimensional
508 reconstructions of mitochondria and cristae after 48-hour treatment with S63845 (MCL1 inhibitor)
509 (scale bar = 0.5μm). (D) Quantification of cristae changes from 3-dimensional reconstruction.
510 Each cristae volume and surface area was normalized to (divided by) the corresponding
511 mitochondrion volume and surface area, respectively, and multiplied by 100 to get the percentage
512 of change. Each data point shown is an individual mitochondrion. Data were analyzed using a
513 parametric two-tailed unpaired t-test with a Welch's correction. (E) Volumetric still frames of
514 mitochondrial cristae 3-D reconstruction of NSCs at 48 hours post-treatment with DMSO control
515 and S63845 (MCL-1 inhibitor) segmented from FIB-SEM volume images. Scale bar = 3000 nm.
516
517 **Figure 3. S63845 and QVD co-treatment reveal altered levels of cristae-shaping proteins.**
518 (A) Schematic detailing the neural induction of human embryonic stem cells (hESCs) using
519 SMADi. hNSCs are maintained in neural induction media (NIM) with daily media changes until
520 they are passaged on day 7. hNSCs are given a 24-hour acclimation period on day 8 before
521 treatment on day 9 with 1μm S63845 (MCL-1 inhibitor), plus or minus 25 μM QVD co-treatment,
522 with DMSO or DMSO+QVD as the control groups. Samples were then collected at 24- and 48-
523 hours post-treatment on days 10 and 11, respectively. Cells were collected in either Trizol for real-
524 time quantitative polymerase chain reaction (RT-qPCR) or protease inhibitor-containing lysis
525 buffer for western blot. (B) Quantified relative expression of *OPA1* and *MIC60* after 24- and 48-
526 hour treatments with DMSO control and S63845 (MCL-1 inhibitor). (C) Left panel: representative
527 images (n=3) of OPA1-L, OPA1-S1, OPA1-S2, MIC60, and MIC10 after 24- and 48-hours of
528 treatment with DMSO control and S63845 (MCL-1 inhibitor). Right panel: quantified band density.
529 (D) Quantified relative expression of *OPA1* and *MIC60* after 24- and 48-hour S63845 plus QVD
530 co-treatment. (E) Representative images (n=3) and quantified band density of OPA1-L, OPA1-

531 S1, OPA1-S2, MIC60, and MIC10 after 24- and 48- hour S63845 plus QVD co-treatment. Each
532 data point represents a biological replicate. Shape of data point corresponds to each biological
533 replicate (circle for n=1, square for n=2, and triangle for n=3). Data analyzed using a parametric
534 two-tailed unpaired t-test with a Welch's Correction. Error bars represent standard error of the
535 mean.
536
537 **Figure 4. S63845 and QVD co-treatment results in downregulation of carnitine**
538 **palmitoyltransferase and altered levels of FAO enzymes.**
539 (A) Schematic of the mitochondrial fatty acid beta-oxidation pathway (B) Quantified relative
540 expression of FAO enzymes after 24- and 48-hours post-treatment with DMSO and S63845
541 (MCL-1 inhibitor). (C) Quantified relative expression of FAO enzymes after 24- and 48-hour
542 S63845 plus QVD co-treatment. (D) Representative images (n=3) and quantified band density of
543 ACSL1, CPT1a, CPT2, and VLCAD after 24- and 48-hours of treatment with DMSO control and
544 S63845 (MCL-1 inhibitor). (E) Representative images (n=3) and quantified band density of
545 ACSL1, CPT1a, CPT2, and VLCAD after 24- and 48- hour S63845 plus QVD co-treatment. Each
546 data point on the graph represents a biological replicate. Shape of data point corresponds to each
547 biological replicate (circle for n=1, square for n=2, and triangle for n=3). Data analyzed using a
548 parametric two-tailed unpaired t-test with Welch's Correction. Error bars represent standard error
549 of the mean.
550
551 **Figure 5. hNSCs supplemented with palmitate and treated with S63845 accumulate lipid**
552 **droplets.**
553 (A) Schematic of experimental design. On day 9 post-induction, hNSCs were treated with S63845
554 in nutrient deficient DMEM media (-glucose, -glutamine, -pyruvate) and supplemented with
555 100μM of palmitate for 12 hours followed by a 2-hour starvation in HBSS. Cells were then live
556 stained with BODIPY and Hoechst prior to PFA fixation. (B) Representative fluorescent images

557 (n=3) of lipid droplets (BODIPY in magenta) and nuclei (Hoechst in cyan) were acquired on a
558 spinning disk confocal microscope at 100X (scale bar = 40μm). (C) Quantification of lipid droplet
559 content, average volume, and maximum volume. Six images were acquired per condition and
560 plotted in gray with shape corresponding to each biological replicate. Each open-shape data point
561 represents the mean per biological replicate. Shape of data point corresponds to each biological
562 replicate (open circle for n=1, open square for n=2, and open triangle for n=3). Means of the
563 biological replicates were analyzed using a parametric two-tailed unpaired t-test with a Welch's
564 Correction. Error bars represent standard error of the mean.
565
566 **Figure 6. S63845 results in depletion of TBR2^{+}/PAX6^{-} IPCs independent of cell death.**
567 Representative fluorescent images (n=3) of nuclear identity markers TBR2 (green), PAX6
568 (magenta), and nuclei (Hoechst in blue) were acquired on a spinning disk confocal microscope at
569 20X (scale bar = 200μm). Intermediate progenitor cells (IPCs) identified by presence of TBR2 and
570 absence of PAX6. (A) Quantified percentage of IPCs after 24- and 48-hour treatments with
571 S63845 (MCL-1 inhibitor). (B) Quantified percentage of IPCs after 24- and 48-hour S63845 plus
572 QVD co-treatment. Quantification of IPCs manually counted and normalized to total cell count for
573 final percentage output. Seven images were acquired per condition and plotted in gray. Each
574 large, open-shape data point represents the mean per biological replicate. Shape of data point
575 corresponds to biological replicate (open circle for n=1, open square for n=2, and open triangle
576 for n=3). Mean of biological replicates analyzed using a two-tailed paired parametric t-test.
577
578 **Figure 7. S63845 results in depletion of BIII-Tubulin^{+} newborn neurons.**
579 (A) Representative fluorescent images of each biological replicate (n=3) of hNSCs treated with
580 S63845 alone or with QVD co-treatment. Newborn neurons labeled with BIII-Tubulin (white) and
581 nuclei (Hoechst in blue) were imaged on a spinning disk confocal microscope at 60X (scale bar =
582 100μm).
583

584 **Acknowledgements**

585 We thank Caleb Hayes, Caroline Bodnya, Meeros Khattaie, Dr. Antentor J. Hinton, Dr. Zer Vue,
586 and Dr. Oleg Kovtun for their technical advice and assistance. This work was supported by 2R35
587 GM128915-01NIGMS (VG), Training Program in Stem Cell and Regenerative Developmental
588 Biology 5T32HD007502-25 (MRH). 2R25GM134979-06 (MY), and HHMI Gilliam Fellowship
589 GT15720 (MG). All TEM and FIB-SEM imaging and image analysis were performed in part using
590 the Vanderbilt Cell Imaging Shared Resource, which is supported by NIH grants 1S10OD012324-
591 01 and 1S10OD021630-01. The authors declare no competing financial interests.

592 **Author contributions**

593 M. R. Hanna and V. Gama conceived the study, designed experiments, interpreted data, and
594 wrote the manuscript. V. Gama supervised the research. M. R. Hanna designed, conducted, and
595 analyzed all cell biology experiments, with technical assistance from M. Gil, M. Yarbrough, and J.
596 Costanzo. E. Krystofiak performed TEM and FIB-SEM tissue preparation and imaging. M.
597 Yarbrough performed 3D reconstruction and analysis of FIB-SEM data. All authors edited the
598 document.

599

References

1. Hansen, D. V., Lui, J. H., Parker, P. R. L. & Kriegstein, A. R. Neurogenic radial glia in the outer subventricular zone of human neocortex. *Nature* **464**, 554–561 (2010).
2. Pollen, A. A., Nowakowski, T. J., Chen, J., Retallack, H., Sandoval-Espinosa, C., Nicholas, C. R., Shuga, J., Liu, S. J., Oldham, M. C., Diaz, A., Lim, D. A., Leyrat, A. A., West, J. A. & Kriegstein, A. R. Molecular Identity of Human Outer Radial Glia during Cortical Development. *Cell* **163**, 55–67 (2015).
3. Beattie, R. & Hippenmeyer, S. Mechanisms of radial glia progenitor cell lineage progression. *FEBS Lett* **591**, 3993–4008 (2017).
4. Silbereis, J. C., Pochareddy, S., Zhu, Y., Li, M. & Sestan, N. The Cellular and Molecular Landscapes of the Developing Human Central Nervous System. *Neuron* **89**, 248–268 (2016).
5. Molnár, Z., Clowry, G. J., Šestan, N., Alzu'bi, A., Bakken, T., Hevner, R. F., Hüppi, P. S., Kostović, I., Rakic, P., Anton, E. S., Edwards, D., Garcez, P., Hoerder-Suabedissen, A. & Kriegstein, A. New insights into the development of the human cerebral cortex. *J Anat* **235**, 432–451 (2019).
6. Haubensak, W., Attardo, A., Denk, W. & Huttner, W. B. Neurons arise in the basal neuroepithelium of the early mammalian telencephalon: A major site of neurogenesis. *Proceedings of the National Academy of Sciences* **101**, 3196–3201 (2004).
7. Yoon, K.-J., Koo, B.-K., Im, S.-K., Jeong, H.-W., Ghim, J., Kwon, M., Moon, J.-S., Miyata, T. & Kong, Y.-Y. Mind Bomb 1-Expressing Intermediate Progenitors Generate Notch Signaling to Maintain Radial Glial Cells. *Neuron* **58**, 519–531 (2008).
8. Englund, C., Fink, A., Lau, C., Pham, D., Daza, R. A. M., Bulfone, A., Kowalczyk, T. & Hevner, R. F. Pax6, Tbr2, and Tbr1 Are Expressed Sequentially by Radial Glia, Intermediate Progenitor Cells, and Postmitotic Neurons in Developing Neocortex. *J. Neurosci.* **25**, 247–251 (2005).
9. Kawaguchi, A., Ikawa, T., Kasukawa, T., Ueda, H. R., Kurimoto, K., Saitou, M. & Matsuzaki, F. Single-cell gene profiling defines differential progenitor subclasses in mammalian neurogenesis. *Development* **135**, 3113–3124 (2008).
10. Tajbakhsh, S. Stem cell: what's in a name? *Nat Rep Stem Cells* 1–1 (2009) doi:10.1038/stemcells.2009.90.
11. Kowalczyk, T., Pontious, A., Englund, C., Daza, R. A. M., Bedogni, F., Hodge, R., Attardo, A., Bell, C., Huttner, W. B. & Hevner, R. F. Intermediate Neuronal Progenitors (Basal Progenitors) Produce Pyramidal–Projection Neurons for All Layers of Cerebral Cortex. *Cerebral Cortex* **19**, 2439–2450 (2009).
12. Hevner, R. F. Intermediate progenitors and Tbr2 in cortical development. *Journal of Anatomy* **235**, 616–625 (2019).
13. Copp, A. J. & Greene, N. D. E. Neural tube defects—disorders of neurulation and related embryonic processes. *WIREs Developmental Biology* **2**, 213–227 (2013).
14. Baum, T. & Gama, V. Dynamic properties of mitochondria during human corticogenesis. *Development* **148**, dev194183 (2021).
15. Robertson, G. L., Riffle, S., Patel, M., Bodnya, C., Marshall, A., Beasley, H. K., Garza-Lopez, E., Shao, J., Vue, Z., Hinton, A., Jr, Stoll, M. S., de Wet, S., Theart, R. P., Chakrabarty, R. P., Loos, B., Chandel, N. S., Mears, J. A. & Gama, V. DRP1 mutations associated with EMPF1 encephalopathy alter mitochondrial membrane potential and metabolic programs. *Journal of Cell Science* **136**, jcs260370 (2023).
16. Colina-Tenorio, L., Horten, P., Pfanner, N. & Rampelt, H. Shaping the mitochondrial inner membrane in health and disease. *Journal of Internal Medicine* **287**, 645–664 (2020).
17. Rasmussen, M. L., Kline, L. A., Park, K. P., Ortolano, N. A., Romero-Morales, A. I., Anthony, C. C., Beckermann, K. E. & Gama, V. A Non-apoptotic Function of MCL-1 in Promoting

Pluripotency and Modulating Mitochondrial Dynamics in Stem Cells. *Stem Cell Reports* **10**, 684–692 (2018).

18. Perciavalle, R. M., Stewart, D. P., Koss, B., Lynch, J., Milasta, S., Bathina, M., Temirov, J., Cleland, M. M., Pelletier, S., Schuetz, J. D., Youle, R. J., Green, D. R. & Opferman, J. T. Anti-apoptotic MCL-1 localizes to the mitochondrial matrix and couples mitochondrial fusion to respiration. *Nature Cell Biology* **14**, 575–583 (2012).
19. Perciavalle, R. M. & Opferman, J. T. Delving deeper: MCL-1's contributions to normal and cancer biology. *Trends in Cell Biology* **23**, 22–29 (2013).
20. Wang, X., Bathina, M., Lynch, J., Koss, B., Calabrese, C., Frase, S., Schuetz, J. D., Rehg, J. E. & Opferman, J. T. Deletion of MCL-1 causes lethal cardiac failure and mitochondrial dysfunction. *Genes Dev* **27**, 1351–1364 (2013).
21. Kozopas, K. M., Yang, T., Buchan, H. L., Zhou, P. & Craig, R. W. MCLI, a gene expressed in programmed myeloid cell differentiation, has sequence similarity to BCL2. *Proc. Natl. Acad. Sci. USA* 5 (1993).
22. Escudero, S., Zaganjor, E., Lee, S., Mill, C. P., Morgan, A. M., Crawford, E. B., Chen, J., Wales, T. E., Mourtada, R., Luccarelli, J., Bird, G. H., Steidl, U., Engen, J. R., Haigis, M. C., Opferman, J. T. & Walensky, L. D. Dynamic Regulation of Long-Chain Fatty Acid Oxidation by a Noncanonical Interaction between the MCL-1 BH3 Helix and VLCAD. *Molecular Cell* **69**, 729-743.e7 (2018).
23. Rasmussen, M. L., Taneja, N., Neininger, A. C., Wang, L., Robertson, G. L., Riffle, S. N., Shi, L., Knollmann, B. C., Burnette, D. T. & Gama, V. MCL-1 Inhibition by Selective BH3 Mimetics Disrupts Mitochondrial Dynamics Causing Loss of Viability and Functionality of Human Cardiomyocytes. *iScience* **23**, (2020).
24. Prew, M. S., Adhikary, U., Choi, D. W., Portero, E. P., Paulo, J. A., Gowda, P., Budhraja, A., Opferman, J. T., Gygi, S. P., Danial, N. N. & Walensky, L. D. MCL-1 is a master regulator of cancer dependency on fatty acid oxidation. *Cell Reports* **41**, 111445 (2022).
25. Wright, T., Turnis, M. E., Grace, C. R., Li, X., Brakefield, L. A., Wang, Y.-D., Xu, H., Kaminska, E., Climer, L. K., Mukiza, T. O., Chang, C.-L., Moldoveanu, T. & Opferman, J. T. Anti-apoptotic MCL-1 promotes long-chain fatty acid oxidation through interaction with ACSL1. *Molecular Cell* **0**, (2024).
26. Brinkmann, K., McArthur, K., Malelang, S., Gibson, L., Tee, A., Elahee Doomun, S. N., Rowe, C. L., Arandjelovic, P., Marchingo, J. M., D'Silva, D., Bachem, A., Monard, S., Whelan, L. G., Dewson, G., Putoczki, T. L., Bouillet, P., Fu, N. Y., Brown, K. K., Kueh, A. J., Wimmer, V. C., Herold, M. J., Thomas, T., Voss, A. K. & Strasser, A. Relative importance of the anti-apoptotic versus apoptosis-unrelated functions of MCL-1 in vivo. *Science* **389**, 1003–1011 (2025).
27. Opferman, J. T., Iwasaki, H., Ong, C. C., Suh, H., Mizuno, S., Akashi, K. & Korsmeyer, S. J. Obligate role of anti-apoptotic MCL-1 in the survival of hematopoietic stem cells. *Science* **307**, 1101–1104 (2005).
28. Opferman, J. T., Letai, A., Beard, C., Sorcinelli, M. D., Ong, C. C. & Korsmeyer, S. J. Development and maintenance of B and T lymphocytes requires antiapoptotic MCL-1. *Nature* **426**, 671–676 (2003).
29. Vikstrom, I., Carotta, S., Lüthje, K., Peperzak, V., Jost, P. J., Glaser, S., Busslinger, M., Bouillet, P., Strasser, A., Nutt, S. L. & Tarlinton, D. M. Mcl-1 is essential for germinal center formation and B cell memory. *Science* **330**, 1095–1099 (2010).
30. Arbour, N., Vanderluit, J. L., Le Grand, J. N., Jahani-Asl, A., Ruzhynsky, V. A., Cheung, E. C. C., Kelly, M. A., MacKenzie, A. E., Park, D. S., Opferman, J. T. & Slack, R. S. Mcl-1 Is a Key Regulator of Apoptosis during CNS Development and after DNA Damage. *Journal of Neuroscience* **28**, 6068–6078 (2008).
31. Rasmussen, M. L., Taneja, N., Neininger, A. C., Wang, L., Robertson, G. L., Riffle, S. N., Shi, L., Knollmann, B. C., Burnette, D. T. & Gama, V. MCL-1 Inhibition by Selective BH3 Mimetics

Disrupts Mitochondrial Dynamics Causing Loss of Viability and Functionality of Human Cardiomyocytes. *iScience* **23**, 101015 (2020).

32. Iwata, R., Casimir, P. & Vanderhaeghen, P. Mitochondrial dynamics in postmitotic cells regulate neurogenesis. *Science* **369**, 858–862 (2020).
33. Takahashi, K. & Yamanaka, S. Induction of Pluripotent Stem Cells from Mouse Embryonic and Adult Fibroblast Cultures by Defined Factors. *Cell* **126**, 663–676 (2006).
34. Takahashi, K., Tanabe, K., Ohnuki, M., Narita, M., Ichisaka, T., Tomoda, K. & Yamanaka, S. Induction of Pluripotent Stem Cells from Adult Human Fibroblasts by Defined Factors. *Cell* **131**, 861–872 (2007).
35. Khacho, M., Clark, A., Svoboda, D. S., Azzi, J., MacLaurin, J. G., Meghaizel, C., Sesaki, H., Lagace, D. C., Germain, M., Harper, M.-E., Park, D. S. & Slack, R. S. Mitochondrial Dynamics Impacts Stem Cell Identity and Fate Decisions by Regulating a Nuclear Transcriptional Program. *Cell Stem Cell* **19**, 232–247 (2016).
36. Iwata Ryohei, Casimir Pierre, & Vanderhaeghen Pierre. Mitochondrial dynamics in postmitotic cells regulate neurogenesis. *Science* **369**, 858–862 (2020).
37. Xie, Z., Jones, A., Deeney, J. T., Hur, S. K. & Bankaitis, V. A. Inborn Errors of Long-Chain Fatty Acid β-Oxidation Link Neural Stem Cell Self-Renewal to Autism. *Cell Rep* **14**, 991–999 (2016).
38. Knobloch, M., Pilz, G.-A., Ghesquière, B., Kovacs, W. J., Wegleiter, T., Moore, D. L., Hruzova, M., Zamboni, N., Carmeliet, P. & Jessberger, S. A Fatty Acid Oxidation-Dependent Metabolic Shift Regulates Adult Neural Stem Cell Activity. *Cell Reports* **20**, 2144–2155 (2017).
39. Stoll, E. A., Makin, R., Sweet, I. R., Trevelyan, A. J., Miwa, S., Horner, P. J. & Turnbull, D. M. Neural Stem Cells in the Adult Subventricular Zone Oxidize Fatty Acids to Produce Energy and Support Neurogenic Activity. *Stem Cells* **33**, 2306–2319 (2015).
40. Khoa, L. T. P., Tsan, Y.-C., Mao, F., Kremer, D. M., Sajjakulnukit, P., Zhang, L., Zhou, B., Tong, X., Bhanu, N. V., Choudhary, C., Garcia, B. A., Yin, L., Smith, G. D., Saunders, T. L., Bielas, S. L., Lyssiotis, C. A. & Dou, Y. Histone Acetyltransferase MOF Blocks Acquisition of Quiescence in Ground-State ESCs through Activating Fatty Acid Oxidation. *Cell Stem Cell* **27**, 441-458.e10 (2020).
41. Schvartzman, J. M., Thompson, C. B. & Finley, L. W. S. Metabolic regulation of chromatin modifications and gene expression. *J Cell Biol* **217**, 2247–2259 (2018).
42. Arnold, P. K., Jackson, B. T., Paras, K. I., Brunner, J. S., Hart, M. L., Newsom, O. J., Alibeckoff, S. P., Endress, J., Drill, E., Sullivan, L. B. & Finley, L. W. S. A non-canonical tricarboxylic acid cycle underlies cellular identity. *Nature* **603**, 477–481 (2022).
43. Ramosaj, M., Madsen, S., Maillard, V., Scandella, V., Sudria-Lopez, D., Yuizumi, N., Telley, L. & Knobloch, M. Lipid droplet availability affects neural stem/progenitor cell metabolism and proliferation. *Nat Commun* **12**, 7362 (2021).
44. Opferman, J. T. & Kothari, A. Anti-apoptotic BCL-2 family members in development. *Cell Death Differ* **25**, 37–45 (2018).
45. Khacho, M. & Slack, R. S. Mitochondrial dynamics in the regulation of neurogenesis: From development to the adult brain. *Developmental Dynamics* **247**, 47–53 (2018).
46. Chambers, S. M., Fasano, C. A., Papapetrou, E. P., Tomishima, M., Sadelain, M. & Studer, L. Highly efficient neural conversion of human ES and iPS cells by dual inhibition of SMAD signaling. *Nat Biotechnol* **27**, 275–280 (2009).
47. Tantawy, S. I., Timofeeva, N., Hernandez, A., Sarkar, A. & Gandhi, V. Decoding the mechanism behind MCL-1 inhibitors: A pathway to understanding MCL-1 protein stability. *Oncotarget* **14**, 653–655 (2023).
48. Eramo, M. J., Lisnyak, V., Formosa, L. E. & Ryan, M. T. The ‘mitochondrial contact site and cristae organising system’ (MICOS) in health and human disease. *J Biochem* **167**, 243–255 (2020).

49. Stephan, T., Brüser, C., Deckers, M., Steyer, A. M., Balzarotti, F., Barbot, M., Behr, T. S., Heim, G., Hübner, W., Ilgen, P., Lange, F., Pacheu-Grau, D., Pape, J. K., Stoldt, S., Huser, T., Hell, S. W., Möbius, W., Rehling, P., Riedel, D. & Jakobs, S. MICOS assembly controls mitochondrial inner membrane remodeling and crista junction redistribution to mediate cristae formation. *EMBO J* **39**, e104105 (2020).
50. Glytsou, C., Calvo, E., Cogliati, S., Mehrotra, A., Anastasia, I., Rigoni, G., Raimondi, A., Shintani, N., Loureiro, M., Vazquez, J., Pellegrini, L., Enriquez, J. A., Scorrano, L. & Soriano, M. E. Optic Atrophy 1 Is Epistatic to the Core MICOS Component MIC60 in Mitochondrial Cristae Shape Control. *Cell Reports* **17**, 3024–3034 (2016).
51. Hu, C., Shu, L., Huang, X., Yu, J., Li, L., Gong, L., Yang, M., Wu, Z., Gao, Z., Zhao, Y., Chen, L. & Song, Z. OPA1 and MICOS Regulate mitochondrial crista dynamics and formation. *Cell Death Dis* **11**, 1–17 (2020).
52. von der Malsburg, A., Sapp, G. M., Zuccaro, K. E., von Appen, A., Moss, F. R., Kalia, R., Bennett, J. A., Abriata, L. A., Dal Peraro, M., van der Laan, M., Frost, A. & Aydin, H. Structural mechanism of mitochondrial membrane remodelling by human OPA1. *Nature* **620**, 1101–1108 (2023).
53. Green, D. R. & Llambi, F. Cell Death Signaling. *Cold Spring Harb Perspect Biol* **7**, a006080 (2015).
54. Iwata, R., Casimir, P., Erkol, E., Boubakar, L., Planque, M., Gallego López, I. M., Ditkowska, M., Gaspariunaite, V., Beckers, S., Remans, D., Vints, K., Vandekeere, A., Poovathingal, S., Bird, M., Vlaeminck, I., Creemers, E., Wierda, K., Corthout, N., Vermeersch, P., Carpentier, S., Davie, K., Mazzone, M., Gounko, N. V., Aerts, S., Ghesquière, B., Fendt, S.-M. & Vanderhaeghen, P. Mitochondria metabolism sets the species-specific tempo of neuronal development. *Science* **379**, eabn4705 (2023).
55. Boassa, D., Deerinck, T. J., Bushong, E. A., Thor, A. & Ellisman, M. Preparation of Cultured Cells for Serial Block Face Scanning Electron Microscopy (SBEM). https://www.protocols.io/view/preparation-of-cultured-cells-for-serial-block-fac-b5naq5ae (2022).
56. Lam, J., Katti, P., Biete, M., Mungai, M., AshShareef, S., Neikirk, K., Garza Lopez, E., Vue, Z., Christensen, T. A., Beasley, H. K., Rodman, T. A., Murray, S. A., Salisbury, J. L., Glancy, B., Shao, J., Pereira, R. O., Abel, E. D. & Hinton, A. A Universal Approach to Analyzing Transmission Electron Microscopy with ImageJ. *Cells* **10**, 2177 (2021).
57. Arzt, M., Deschamps, J., Schmied, C., Pietzsch, T., Schmidt, D., Tomancak, P., Haase, R. & Jug, F. LABKIT: Labeling and Segmentation Toolkit for Big Image Data. *Front. Comput. Sci.* **4**, (2022).
58. Vue, Z., Garza-Lopez, E., Neikirk, K., Katti, P., Vang, L., Beasley, H., Shao, J., Marshall, A. G., Crabtree, A., Murphy, A. C., Jenkins, B. C., Prasad, P., Evans, C., Taylor, B., Mungai, M., Killion, M., Stephens, D., Christensen, T. A., Lam, J., Rodriguez, B., Phillips, M. A., Daneshgar, N., Koh, H., Koh, A., Davis, J., Devine, N., Saleem, M., Scudese, E., Arnold, K. R., Vanessa Chavarin, V., Daniel Robinson, R., Chakraborty, M., Gaddy, J. A., Sweetwyne, M. T., Wilson, G., Zaganjor, E., Kezos, J., Dondi, C., Reddy, A. K., Glancy, B., Kirabo, A., Quintana, A. M., Dai, D., Ocorr, K., Murray, S. A., Damo, S. M., Exil, V., Riggs, B., Mobley, B. C., Gomez, J. A., McReynolds, M. R. & Hinton, A. 3D reconstruction of murine mitochondria reveals changes in structure during aging linked to the MICOS complex. *Aging Cell* **22**, e14009 (2023).

Figure 1

A

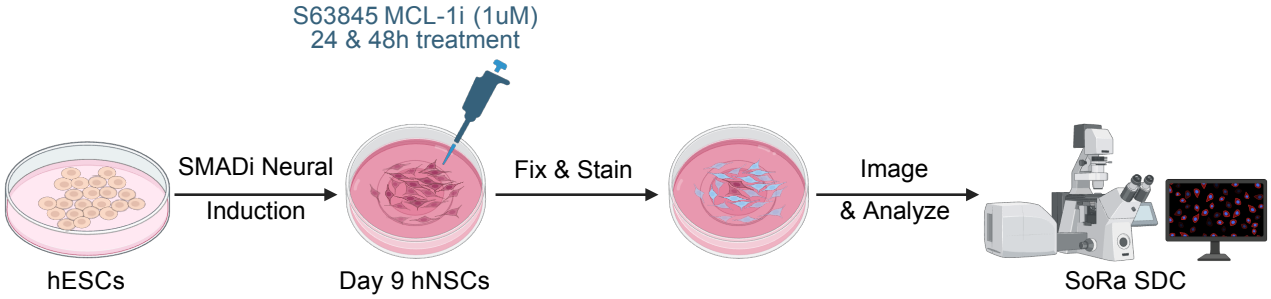
S63845 MCL-1i (1uM)
24 & 48h treatment
SMADi Neural
Induction
Fix & Stain
Image
& Analyze
hESCs
Day 9 hNSCs
SoRa SDC

B

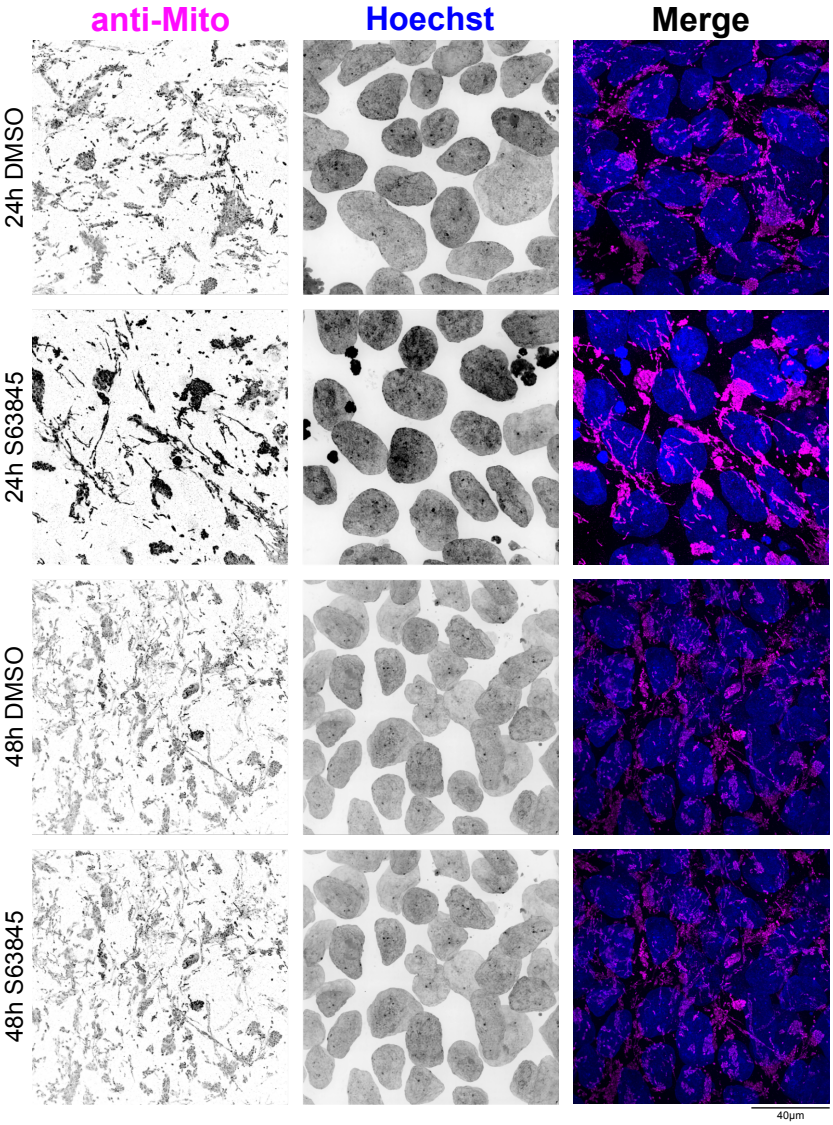
anti-Mito
Hoechst
Merge
24h DMSO
24h S63845
48h DMSO
48h S63845
40µm

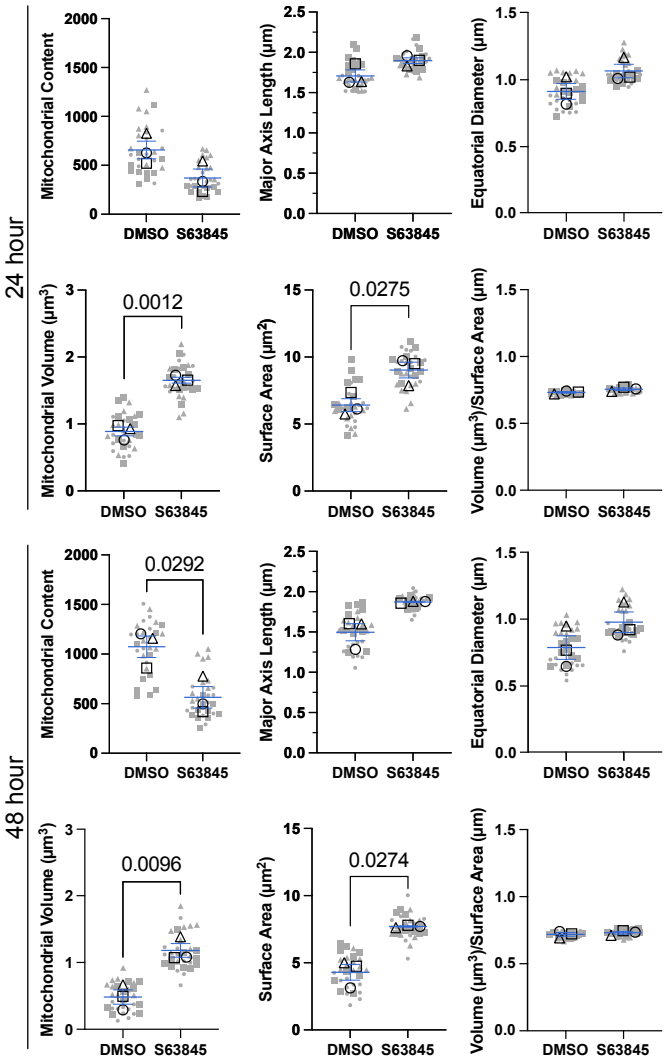
24 hour
48 hour
Mitochondrial Content
Major Axis Length (µm)
Equatorial Diameter (µm)
Mitochondrial Volume (µm³)
Surface Area (µm²)
Volume (µm³)/Surface Area (µm)
DMSO
S63845
0.0012
0.0275
0.0292
0.0096
0.0274

Figure 2

A

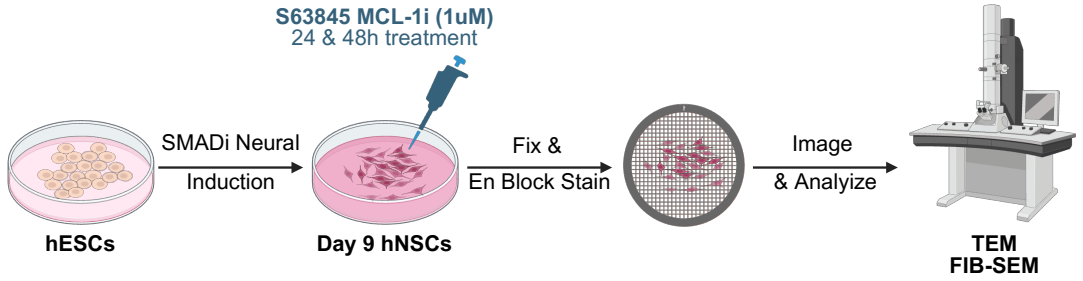

B

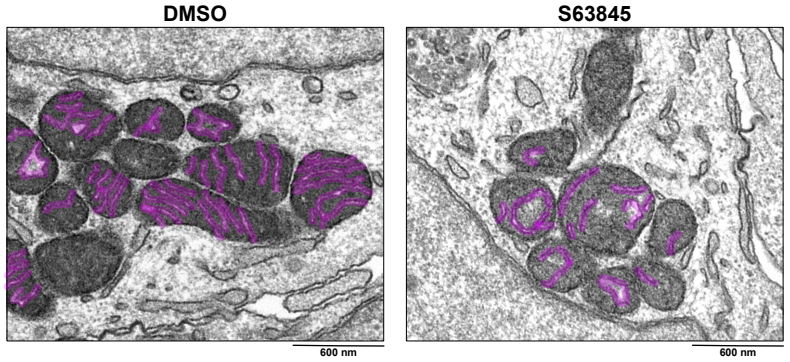

C

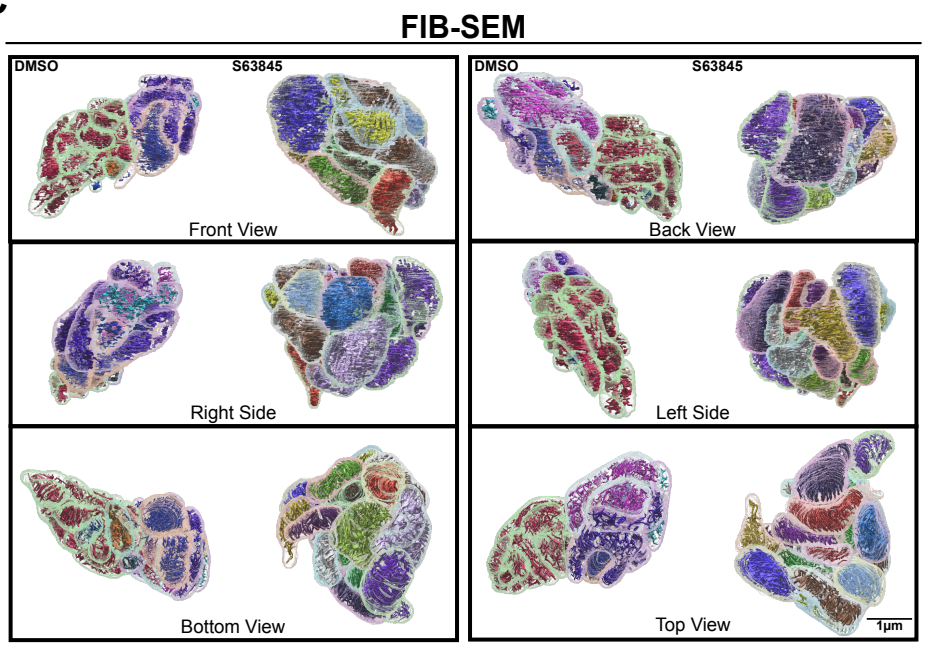

D

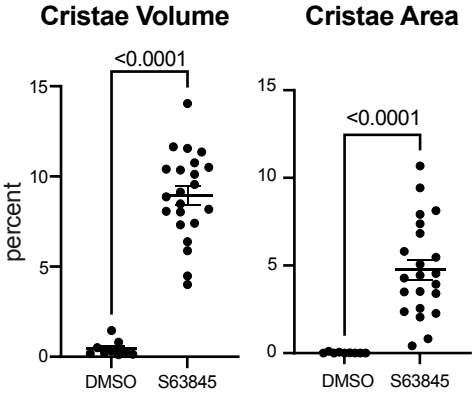

E

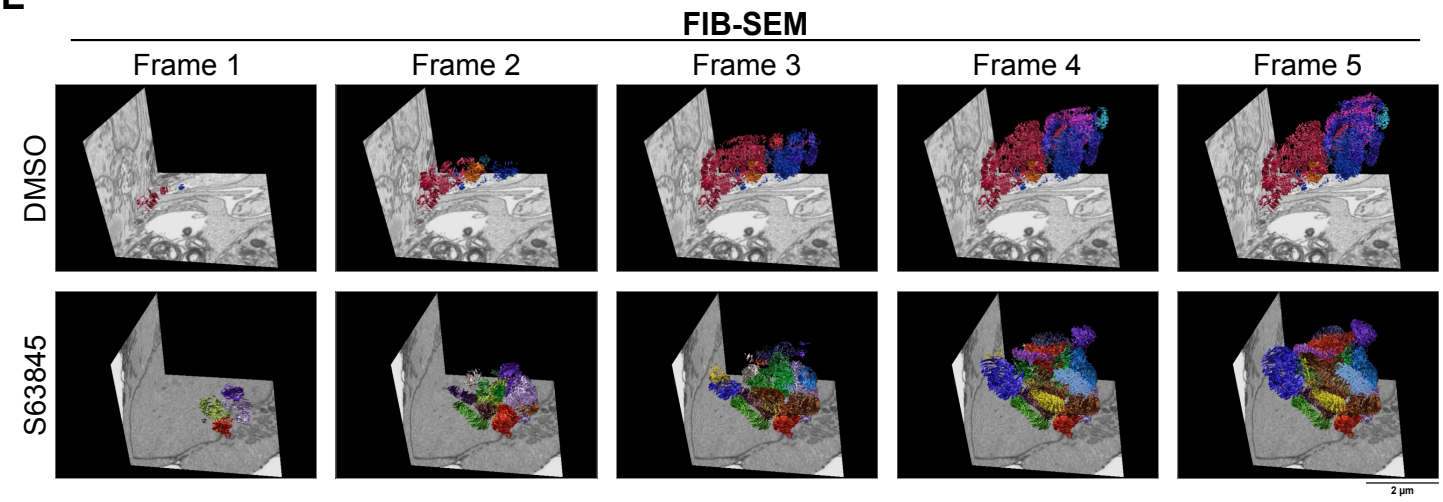

Figure 3

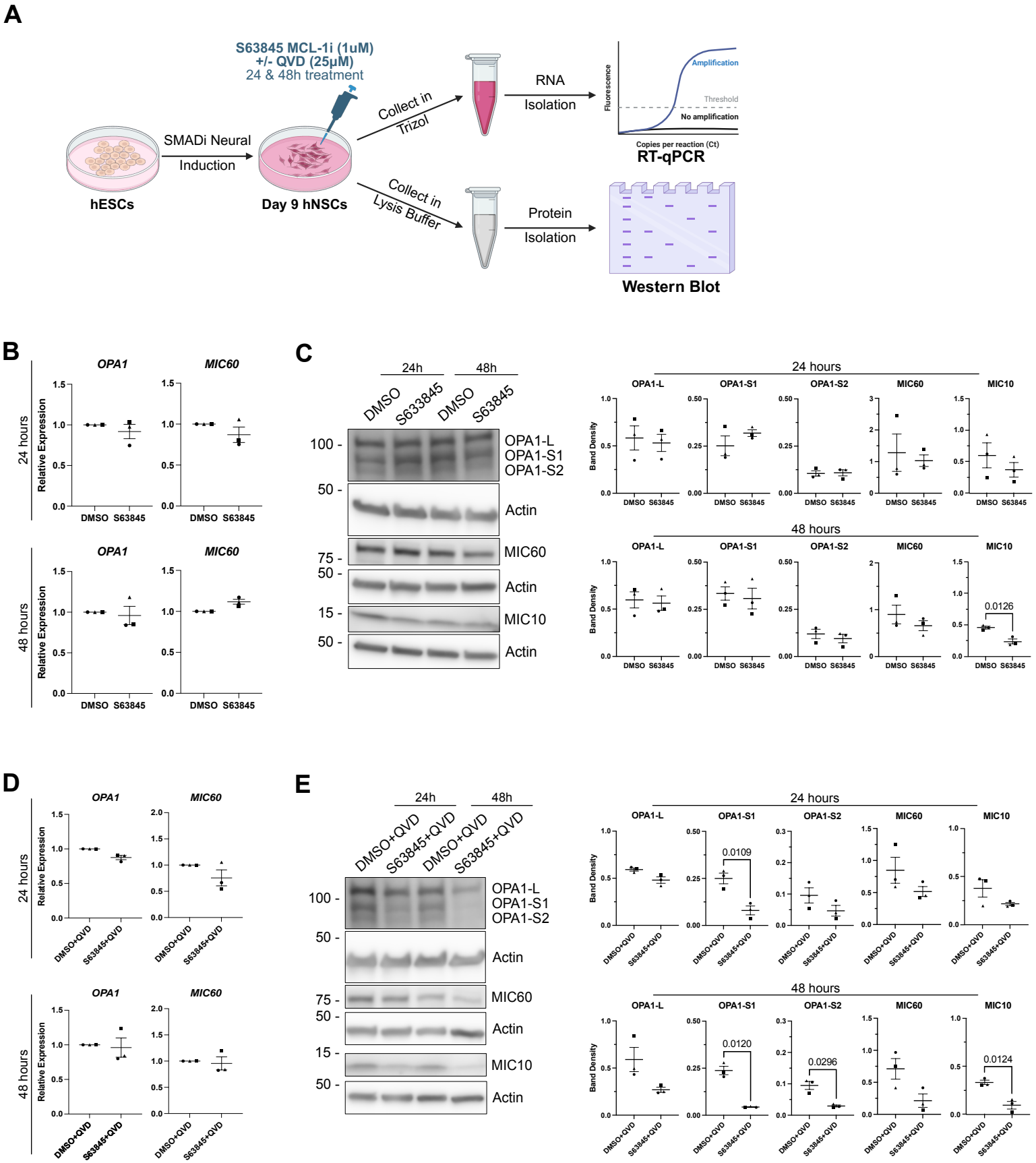
A
S63845 MCL-1i (1uM)
+/- QVD (25μM)
24 & 48h treatment
SMADi Neural
Induction
hESCs
Day 9 hNSCs
Collect in
Trizol
Collect in
Lysis Buffer
RNA
Isolation
Protein
Isolation
Amplification
Threshold
No amplification
Fluorescence
Copies per reaction (Ct)
RT-qPCR
Western Blot
B
OPA1
MIC60
24 hours
48 hours
Relative Expression
DMSO
S63845
C
24h
48h
DMSO
S633845
S63845
OPA1-L
OPA1-S1
OPA1-S2
Actin
MIC60
MIC10
Band Density
0.0126
D
DMSO+QVD
S63845+QVD
E
0.0109
0.0120
0.0296
0.0124

Figure 4

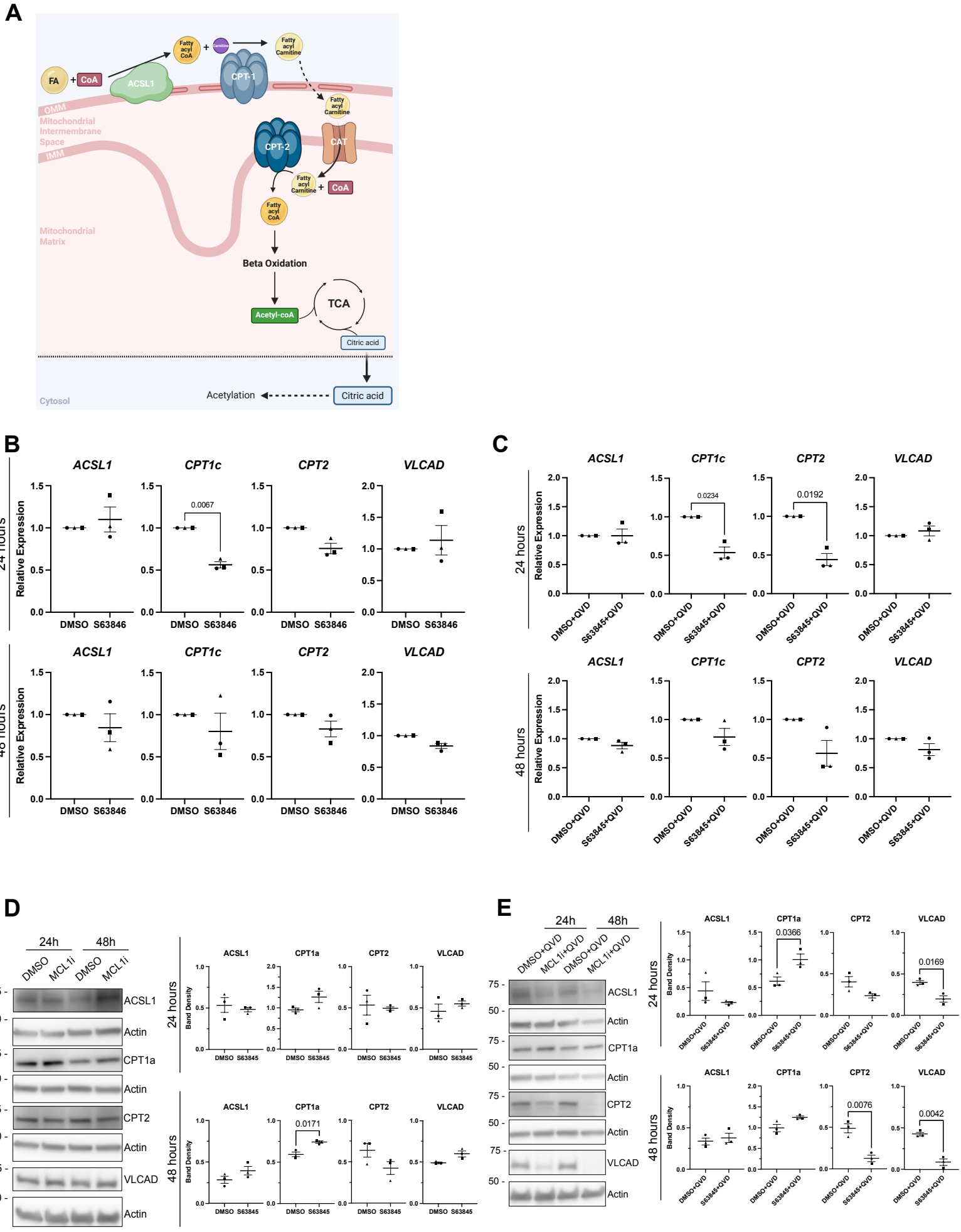
A
FA
CoA
ACSL1
Fatty acyl CoA
Carnitine
CPT-1
Fatty acyl Carnitine
OMM
Mitochondrial Intermembrane Space
IMM
CPT-2
CAT
Fatty acyl Carnitine
CoA
Fatty acyl CoA
Mitochondrial Matrix
Beta Oxidation
Acetyl-coA
TCA
Citric acid
Cytosol
Acetylation
Citric acid
B
24 hours
48 hours
Relative Expression
ACSL1
CPT1c
CPT2
VLCAD
0.0067
DMSO
S63846
C
0.0234
0.0192
DMSO+QVD
S63845+QVD
D
24h
48h
DMSO
MCL1i
ACSL1
Actin
CPT1a
CPT2
VLCAD
Band Density
CPT1a
0.0171
S63845
E
DMSO+QVD
MCL1i+QVD
0.0366
0.0169
0.0076
0.0042

Figure 5

A

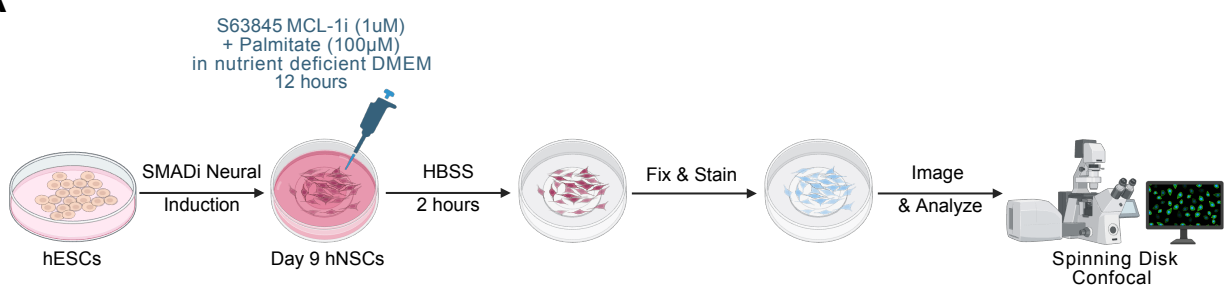
S63845 MCL-1i (1uM)
+ Palmitate (100μM)
in nutrient deficient DMEM
12 hours
SMADi Neural
Induction
HBSS
2 hours
Fix & Stain
Image
& Analyze
hESCs
Day 9 hNSCs
Spinning Disk
Confocal

B

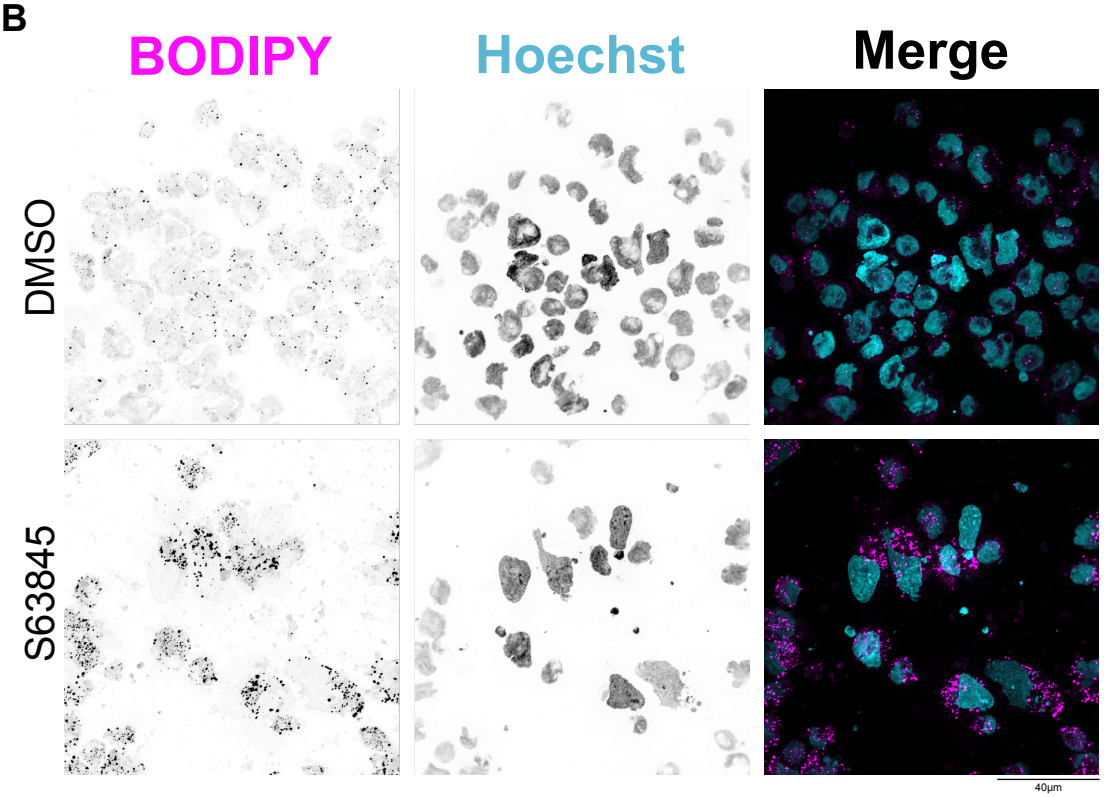
BODIPY
Hoechst
Merge
DMSO
S63845
40μm

C

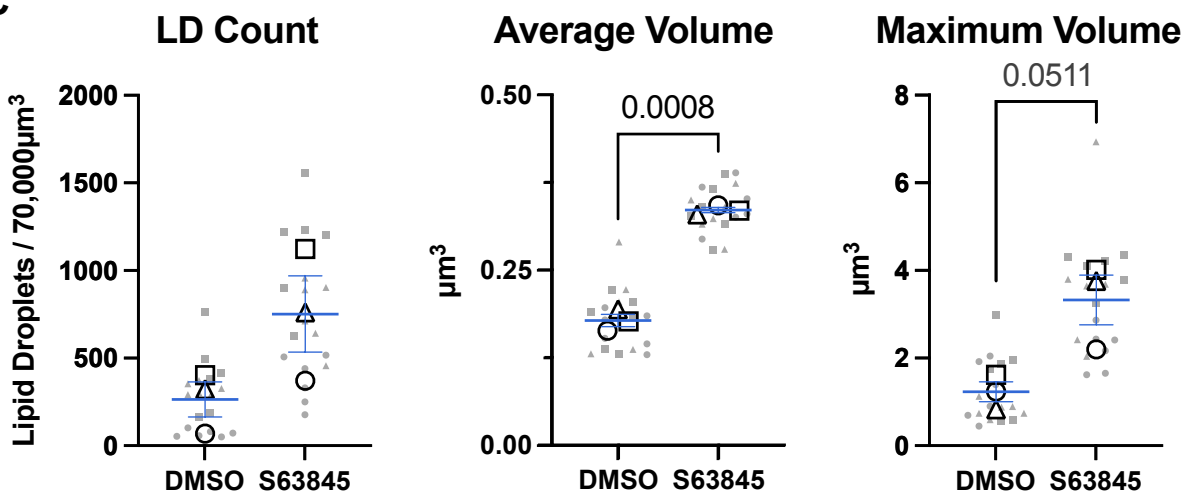
LD Count
Average Volume
Maximum Volume
Lipid Droplets / 70,000μm³
2000
1500
1000
500
0
DMSO
S63845
0.50
0.25
0.00
μm³
0.0008
8
6
4
2
0
0.0511

Figure 6

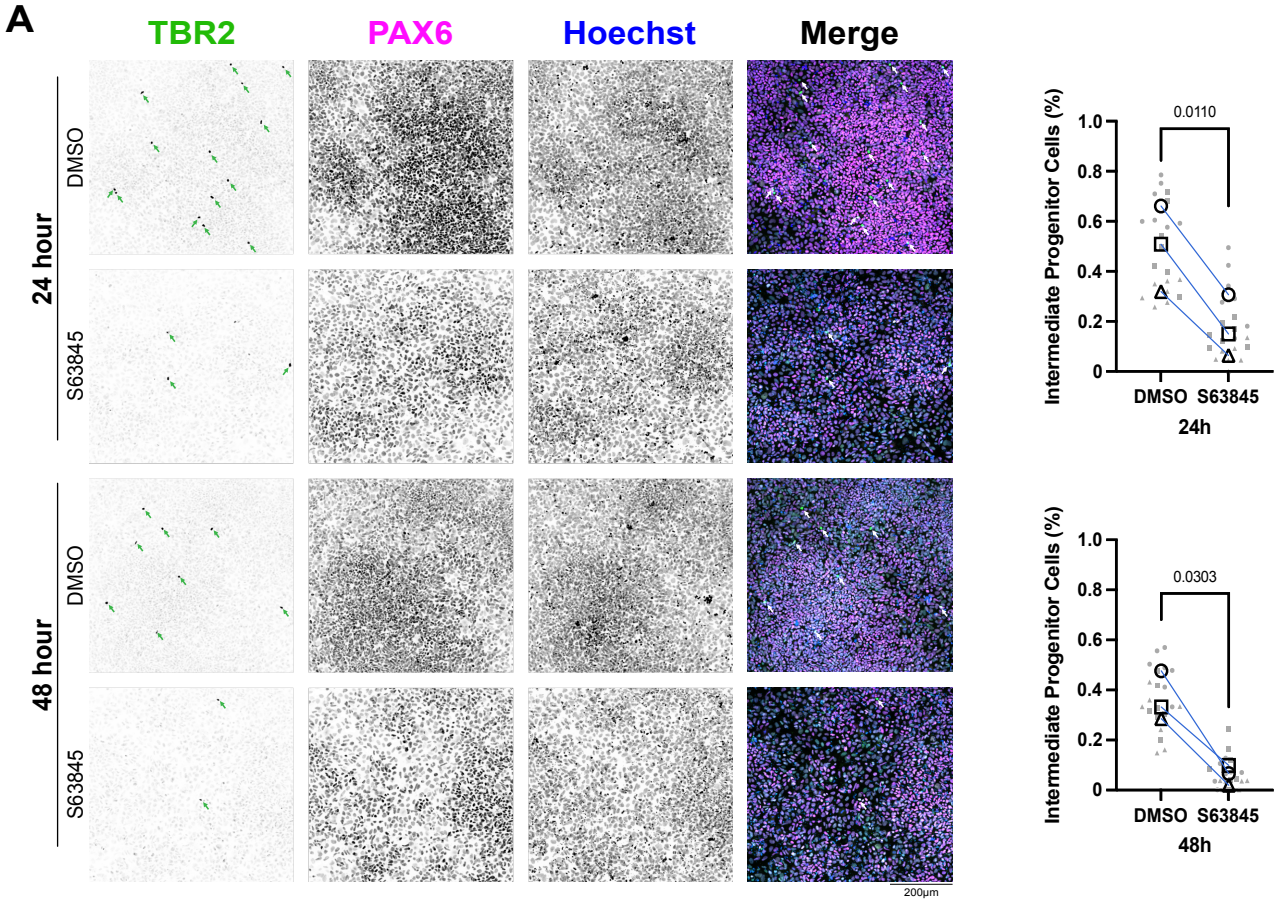
A
TBR2
PAX6
Hoechst
Merge
24 hour
DMSO
S63845
48 hour
DMSO
S63845
200µm
Intermediate Progenitor Cells (%)
0.0110
DMSO
S63845
24h
0.0303
48h

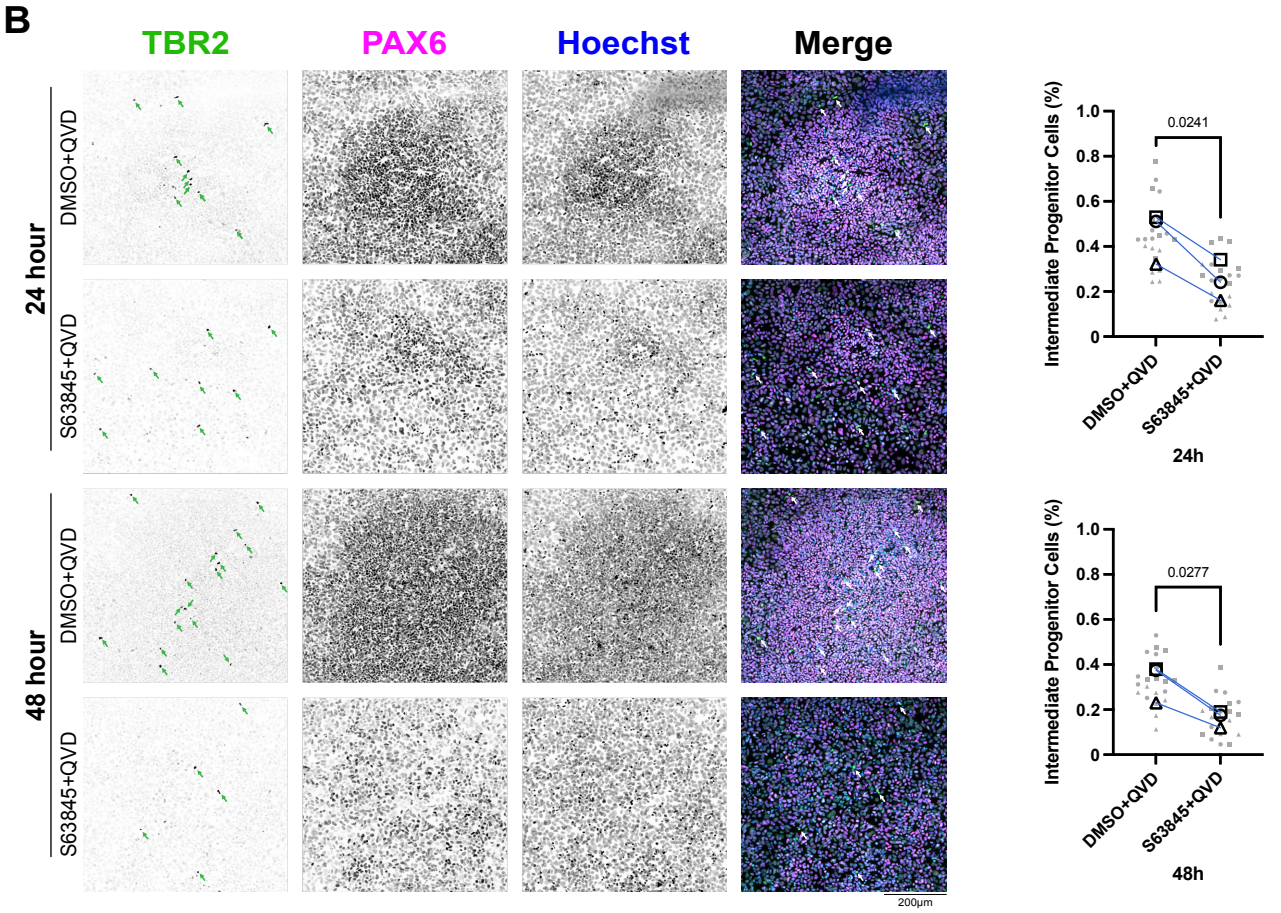
B
TBR2
PAX6
Hoechst
Merge
24 hour
DMSO+QVD
S63845+QVD
48 hour
DMSO+QVD
S63845+QVD
200µm
Intermediate Progenitor Cells (%)
0.0241
DMSO+QVD
S63845+QVD
24h
0.0277
48h

Figure 7

A

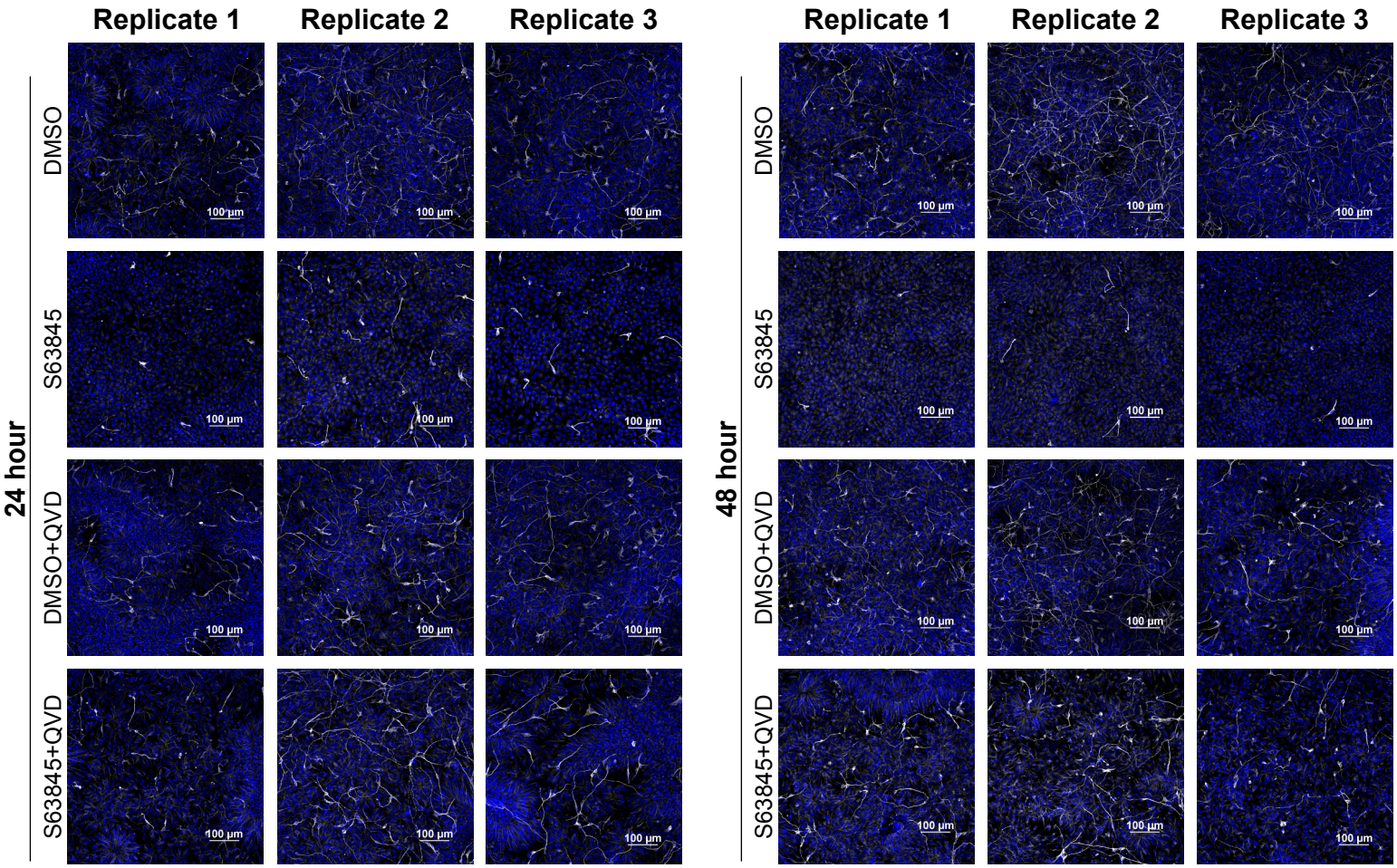
Replicate 1
Replicate 2
Replicate 3
24 hour
48 hour
DMSO
S63845
DMSO+QVD
S63845+QVD
100 µm